Recent Progress and Approaches on Transition Metal Chalcogenides for Hydrogen Production

Sivagowri Shanmugaratnam [1,2], Elilan Yogenthiran [3], Ranjit Koodali [4,*], Punniamoorthy Ravirajan [1], Dhayalan Velauthapillai [2] and Yohi Shivatharsiny [3,*]

1 Clean Energy Research Laboratory (CERL), Department of Physics, University of Jaffna, Jaffna 40000, Sri Lanka; Sivagowrishanmugaratnam@gmail.com (S.S.); pravirajan@univ.jfn.ac.lk (P.R.)
2 Faculty of Engineering and Science, Western Norway University of Applied Sciences, P.O. Box 7030, 5020 Bergen, Norway; Dhayalan.Velauthapillai@hvl.no
3 Department of Chemistry, University of Jaffna, Jaffna 40000, Sri Lanka; elilchem01@gmail.com
4 Department of Chemistry, Western Kentucky University, 1906 College Heights Blvd., Bowling Green, KY 42101, USA
* Correspondence: ranjit.koodali@wku.edu (R.K.); yshiva@univ.jfn.ac.lk (Y.S.)

Abstract: Development of efficient and affordable photocatalysts is of great significance for energy production and environmental sustainability. Transition metal chalcogenides (TMCs) with particle sizes in the 1–100 nm have been used for various applications such as photocatalysis, photovoltaic, and energy storage due to their quantum confinement effect, optoelectronic behavior, and their stability. In particular, TMCs and their heterostructures have great potential as an emerging inexpensive and sustainable alternative to metal-based catalysts for hydrogen evolution. Herein, the methods used for the fabrication of TMCs, characterization techniques employed, and the different methods of solar hydrogen production by using different TMCs as photocatalyst are reviewed. This review provides a summary of TMC photocatalysts for hydrogen production.

Keywords: transition metal chalcogenides; hydrogen production; photocatalysis; apparent quantum yield

1. Introduction

Renewably produced hydrogen gas is used as an alternative clean fuel for transportation. It is regarded as a clean and efficient carrier of energy and is considered as an ideal alternative to fossil fuels to meet the growing energy demand and address environmental issues [1]. When compared with other combustible fuels (i.e., deposited fossil fuels such as coal, oil, and natural gas [2]) hydrogen possesses a high energy density (140 MJkg^{-1}) and the end product of this combustion reaction is only water [3,4]. Therefore, the growing energy demand requires developments in the storage of hydrogen, their transport, and production techniques. Although great progress has been made in H$_2$ storage [5–7] and transport, the utilization of H$_2$ energy is stymied by the lack of inexpensive and efficient production methods [8]. Hydrogen can be produced in different ways (Figure 1) including steam-methane reforming of natural gas, coal gasification, and biomass conversion [9], which are expensive and produce greenhouse gases such as carbon monoxide and carbon dioxide that are not favorable to the environment [10,11]. An attractive alternative technique, solar assisted water splitting, is considered as one of the most suitable and greener ways to produce hydrogen energy [12] and the technology of water splitting becomes mature day-by-day [13].

The simple method for the separation of water is electrolysis and various clean energy resources such as solar, geothermal, biomass, wind, ocean, or other renewables can be used for this process. Among them, using solar energy, water can be split by two methods: photoelectrochemical and photocatalytic water splitting.
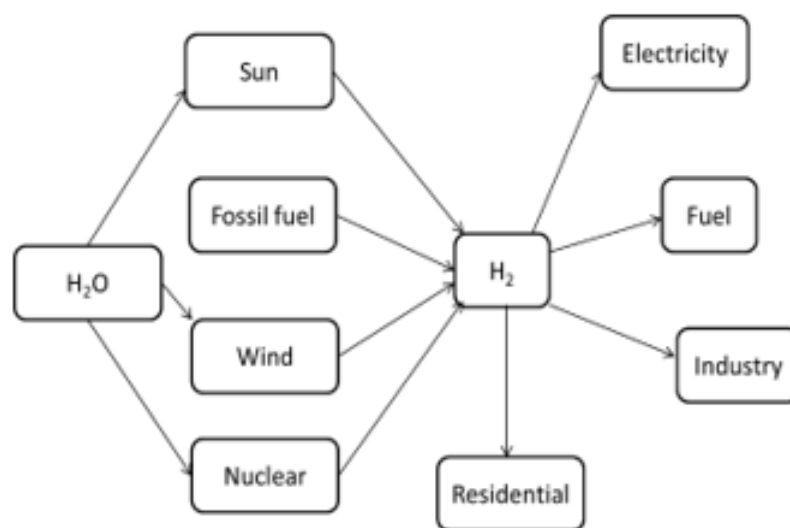
Figure 1. Web-diagram showing the primary energy sources for the production of hydrogen and its uses.

Various types of photocatalytic materials have been utilized for photocatalytic applications. TiO_2 [14–17], ZnO [18], mixed oxide materials [19], perovskite [20,21], dye [22], and metal-doped oxide materials [23,24] are some of them. Among these, transition metal chalcogenides (TMCs) have gained worldwide attention due to their electrocatalytic properties that include indirect band gaps, optoelectronic behavior, and their stability [25]. In addition, nanodots (quantum dots)/nano structures of metal chalcogenides show enhanced catalytic activity at the edges. Furthermore, by limiting their particle size in the 1–10 nm range, due to the quantum confinement effect, it is possible to utilize under solar simulated irradiation [26,27]. Generation of exciton pairs and the effective charge separation in these semiconductor photocatalysts lead to an effective photolysis process. The efficiency of charge transport mainly depends on the crystallinity, particle, and crystallite size of the materials among many other factors. Composites of TMCs with co-catalysts such as graphene [28], graphene oxides [29], carbon nitride [30], metal oxides [19,31–33], $CdLa_2S_4$ [34], and metals [35] have been found to increase the conductivity of electrons, provide active sites, and effectively separate the electron and hole pairs generated by bandgap irradiation of the semiconductor photocatalysts. This review mainly focuses on the synthesis and characterization of various types of TMCs and their application in hydrogen energy production through water splitting. This review may assist researchers by providing insights on the fabrication of highly efficient photocatalysts with low cost and high efficiency.

2. Transition Metal Chalcogenides (TMCs)

TMCs have gained worldwide attention in recent decades. These catalysts have been used in lithium-ion batteries, solar cells, and hydrogen evolution reactions. TMCs can be excited by solar simulated irradiation and due to their indirect band gaps, optoelectronic behavior, small bandgap, and their stability are favorable candidates as photocatalysts. Nowadays, many researchers have focused on the production and photocatalytic activity of TMCs. These TMCs have been synthesized by different techniques that include single-step hydrothermal synthesis [13,36,37], solvothermal method [38], sulfidation and selenization [39], free intercalation method [40], electrospinning technique, the successive ionic layer adsorption and reaction (SILAR) method [32], ultrasonic-exfoliation [23], electrodeposition method [27,41], photoreduction method [42], refluxing method [43], chemical vapor deposition (CVD) [44], template-free one-pot method [45], successive surface modification method [46], and microwave-assisted synthesis [47–50]. The following section will elaborate on some of the above-mentioned synthesis methods in detail.

2.1. Synthesis Methods

2.1.1. Hydrothermal/Solvothermal Method

The hydrothermal technique is one of the frequently reported methods to produce nanomaterials with various morphologies and thicknesses [51]. This method involves a heterogeneous reaction in the presence of an aqueous solvent or mineralizers under high pressure and low temperature to dissolve and recrystallize the materials that are moderately insoluble under ordinary conditions in closed steel containers called autoclaves. If the water is used as the solvent, this process is called the hydrothermal method whereas in the solvothermal method, organic solvents are used [36,52]. This method can be used to synthesize nanomaterials with high crystallinities, favorable crystal facets, tunable morphologies, and controllable sizes by varying experimental factors such as temperature, solvent, time, etc. Hydrothermal synthesis consumes relatively low energy, and most importantly, it is an environmentally friendly method [53,54], and hence is a very common method. Figure 2 illustrates an example of the synthesis of MoS_2.
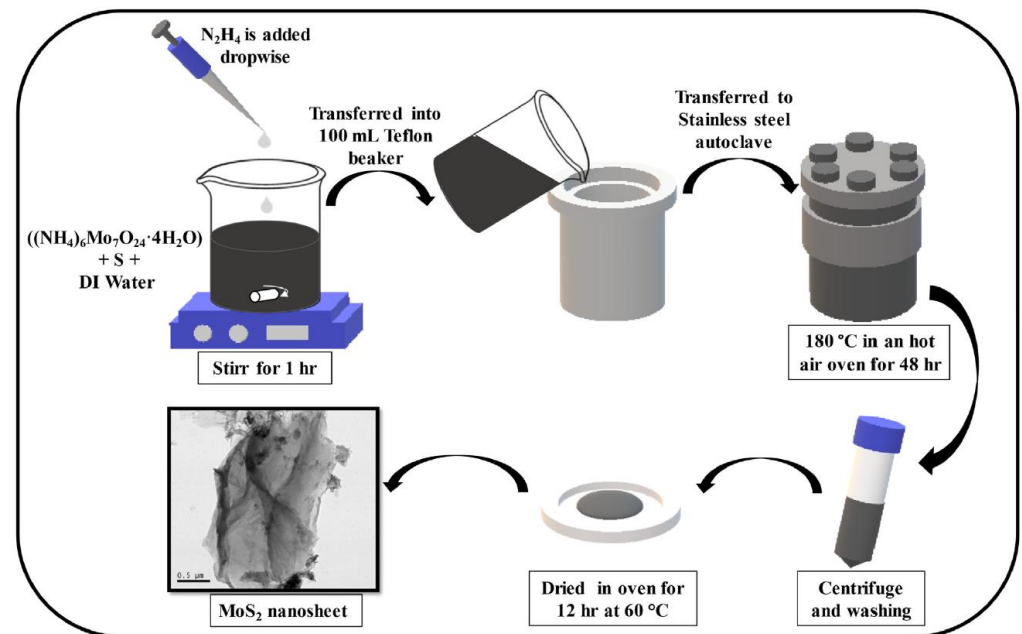

Figure 2. Schematic illustration of synthesis of MoS_2 by the hydrothermal method. Reproduced with permission from [55].

Figure 2 depicts the flow diagram of the synthesis of MoS_2 by the hydrothermal method. Here, ammonium-hepta molybdate tetrahydrate and sulfur (S) powder were used as precursors. The black precipitates were collected and dried to obtain the required MoS_2 sample, which exhibited a layered structure [55].

In a different study, Jing Yu et al. synthesized SnS_2 nanosheets by the solvothermal method. The mechanism of their synthesis is illustrated in Figure 3, where Sn^{2+} from $SnCl_2$ reacts with S^{2-} to form orthorhombic SnS micro flowers stacked with decentralized sheets, and further addition of a S^{2-} source results in SnS_2 with an increase in the reaction time [38].
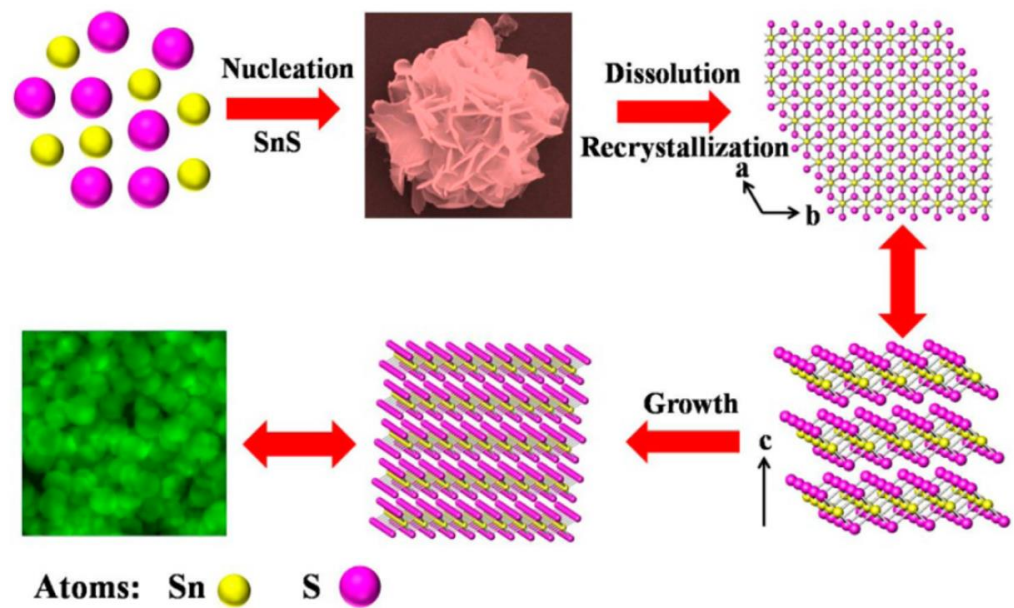
Figure 3. Formation mechanism of SnS$_2$ nanostructures during the solvothermal process. Reproduced with permission from [38].

In addition, surfactants such as SDS (sodium dodecyl sulfate), CTAB (cetyltrimethylammonium bromide), PVP (polyvinyl pyrrolidone) [56], etc. have been used to increase the crystal growth of the nanomaterials, and a hydrothermal synthesis of a WS$_2$ nanosphere by the addition of CTAB is discussed in Figure 4.
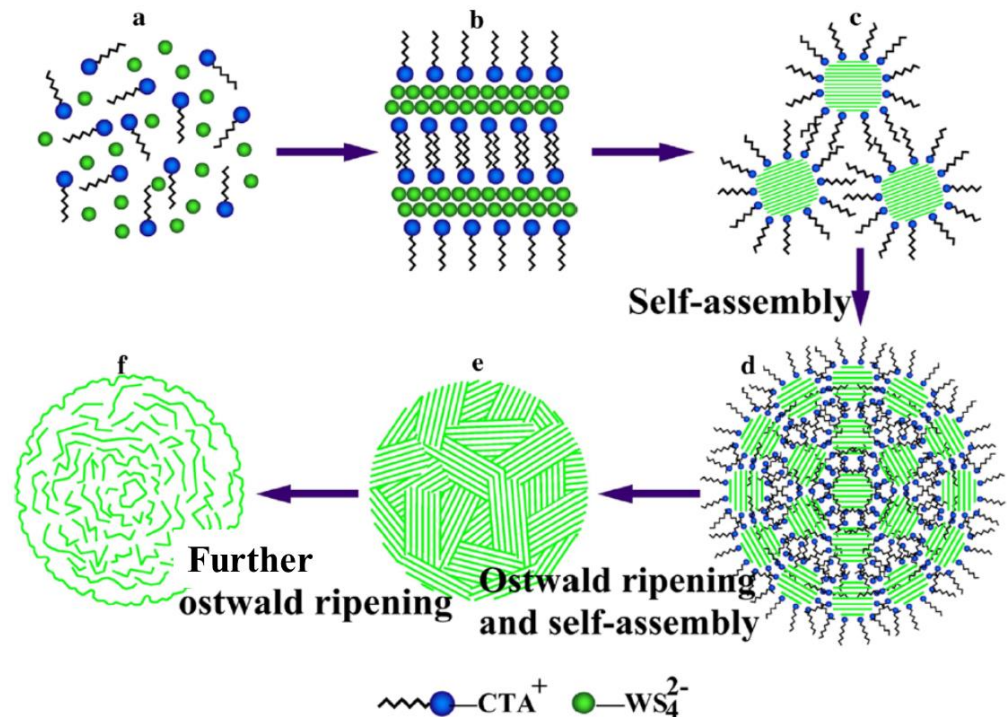
Figure 4. Schematic diagram of the formation process of flower-like WS$_2$ nanospheres using CTAB as aa surfactant. Reproduced with permission from [57].

Figure 4a shows that the CTAB molecules were randomly dispersed in solution as single molecules (not aggregates) at low concentrations under the hydrothermal condition. After the amount of CTAB was adjusted to 1.5 mmol, a lamellar micelle was formed to minimize the free energy of the system. The external surface of the lamellar micelle contains

a hydrophilic head, whereas the tail, which is hydrophobic, points to the micelle center [58]. In Figure 4b, WS_4^{2-} ions tend to form lamellar micelles due to complementary electrostatic interactions between the CTA^+ and WS_4^{2-} To keep the free energy of the system low, the lamellar micelle was formed as an ordered nano-microstructure, as indicated in Figure 4c. Figure 4d shows 3-D assemblies formed through van der Waals forces. Similar methods have been utilized to synthesize FeS_2, NiS_2, and CuS in a different work [37]. The WS_2 nanocrystal was formed from the reduction of WS_4^{2-} ions, as indicated in Figure 4e. The aggregation of WS_2 colloids reduced the surface free energy and formed nanosheets. The flower-like WS_2 nanospheres were obtained as indicated in Figure 4f, and it was concluded that hydrothermal synthesis in the presence of a surfactant such as CTAB and careful control of the precursor concentration can be utilized to obtain the desired flower-like structure [57].

Apart from this hydrothermal method, there is a clean, ultrafast (60 s) synthetic technique that can be conducted using microwave heating without any inert gas protection to achieve uniform TMCs [48,59].

2.1.2. Microwave-Assisted Synthesis

The microwave-assisted synthesis method has also been used to prepare TMCs with controllable sizes and shapes [60]. Figure 5 illustrates the microwave-assisted synthesis of a MoS_2/graphene composite in the presence of ammonium tetrathiomolybdate (ATTM) and CS_2 on a graphene support. The reaction was carried out in a glass vial with equimolar amounts of ATTM and graphene. The reactants were mixed at a constant speed, and then the CS_2 solvent (200 µL) was added and mixed well. The solvent was evaporated after 10 min of air drying. Then, the mixture was kept under microwave irradiation. Here, the graphene served as a substrate to absorb the microwave energy and convert the incident radiation energy to heat. During the process, ATTM was reduced first to MoO_2, and then converted to MoS_2, as indicated in Figure 5 [47].
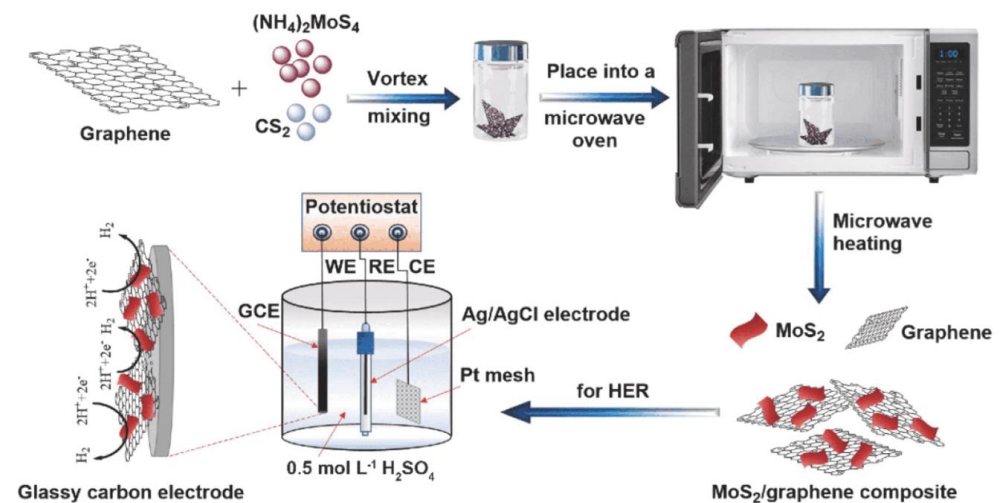

Figure 5. Schematic illustration of the microwave-assisted synthesis of the MoS_2/graphene composite. Reproduced with permission from [47].

In different works, SnS_2 [61], CdS [62], CuS [63], NiS_2 [64], WS_2 [59], and CoS_2 [65] nanomaterials were synthesized using the microwave-assisted synthesis method.

2.1.3. Electrodeposition Method

Electrodeposition is a well-established technique for the preparation of nanomaterials for a wide range of materials (e.g., metal nanoparticles, nanosheet arrays [66], nanowires [67], nanofilms [68], laminated composites [69], multilayered composite coatings [70], and nanoparticle-reinforced composite coatings [71]) and this is a rapid and single-step process. It can be used to produce homogeneous and high-purity crystalline

materials at the cathode of the electrochemical system during the coating process because of the external current (direct or pulsed) applied to the electrodeposition system [72–74].

Figure 6 illustrates the synthesis of MoS_2 quantum dots (QDs) on TiO_2 nano-tube arrays (NTAs) to form heterostructures using a facile electrodeposition method with a three-electrode system. TiO_2 NTAs/Ti foil, Pt foil, and saturated Ag/AgCl electrodes were used as the working electrode, counter electrode, and reference electrode, respectively. MoS_2 QD solution and citric acid–sodium citrate buffer solution (0.1 M, pH 4.5) with a volume ratio of 1:1 was used as the electrolyte of this system. MoS_2 QDs were deposited onto TiO_2 NTA photoelectrodes by the electrodeposition process, and the obtained samples were rinsed with deionized water and dried at ambient temperature after different electrodeposition times of 5, 10, 20, and 30 min., respectively [27].
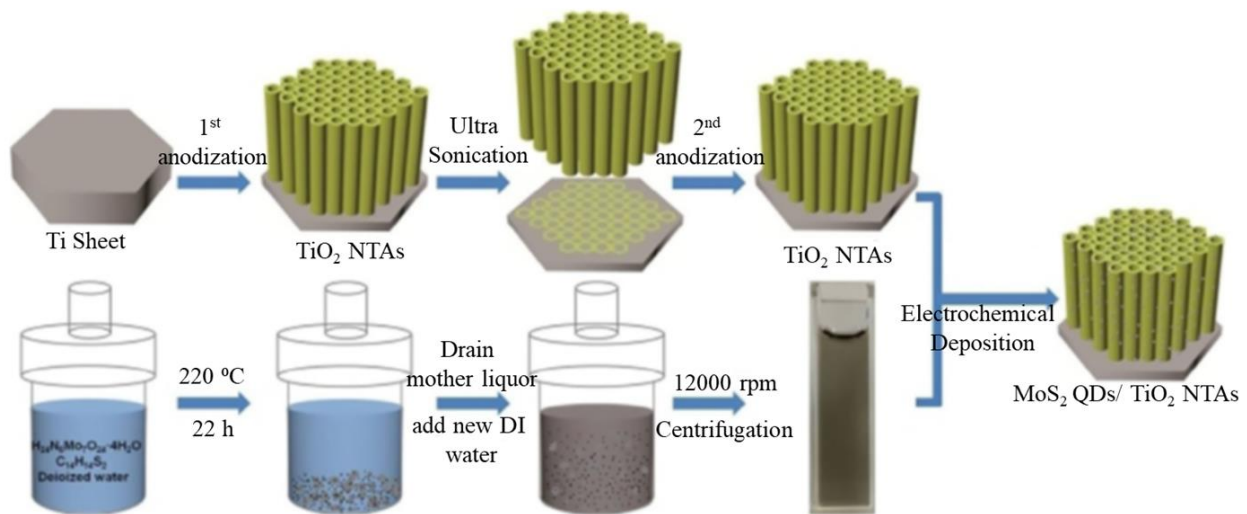

Figure 6. Schematic illustration of the preparation of TiO_2 NTAs, MoS_2 QDs, and MoS_2 QDs@TiO_2 NTA heterostructures. Reproduced with permission from [27].

2.1.4. Photoreduction

Photoreduction, for example, the photodeposition of MoS_2 on rGO_x/CdS was also utilized to prepare metal chalcogenide materials. An appropriate amount of precursor molecule (MoS_4^{2-}) and surfactants were added and the pH of the solution was adjusted by adding an acid or base. Then, the suspension was bubbled with nitrogen to maintain an inert environment, then irradiated with a 350 W Xe lamp equipped with a cutoff filter ($\lambda \geq 420$ nm) for a particular time interval. The incident intensity was 34 mWcm^{-1}. The MoS_4^{2-} ions were reduced to MoS_2 by the photoexcited electrons of rGO_x/CdS. The final product, MoS_2/rGO_x/CdS, was obtained by filtration. The loaded amount of MoS_2 was determined by measuring the MoS_4^{2-} concentrations in both the reacted solution and the washed solution on a spectrophotometer at the wavelength of 468 nm [42].

2.1.5. Electron Beam Evaporation

There have been various methods used in the preparation of Au deposited on a NP/Zn_xCd_{1-x}S NW heterostructure. Ternary Zn_xCd_{1-x}S nanowires were synthesized by using silicon (100) wafers as substrates (Figure 7). First, Au film was deposited on a Si substrate by the electron beam evaporation method. The substrates coated with 10 nm of Au film were placed into the downstream region of a three-zone horizontal quartz tube furnace and then annealed at 500 °C for 1 h.
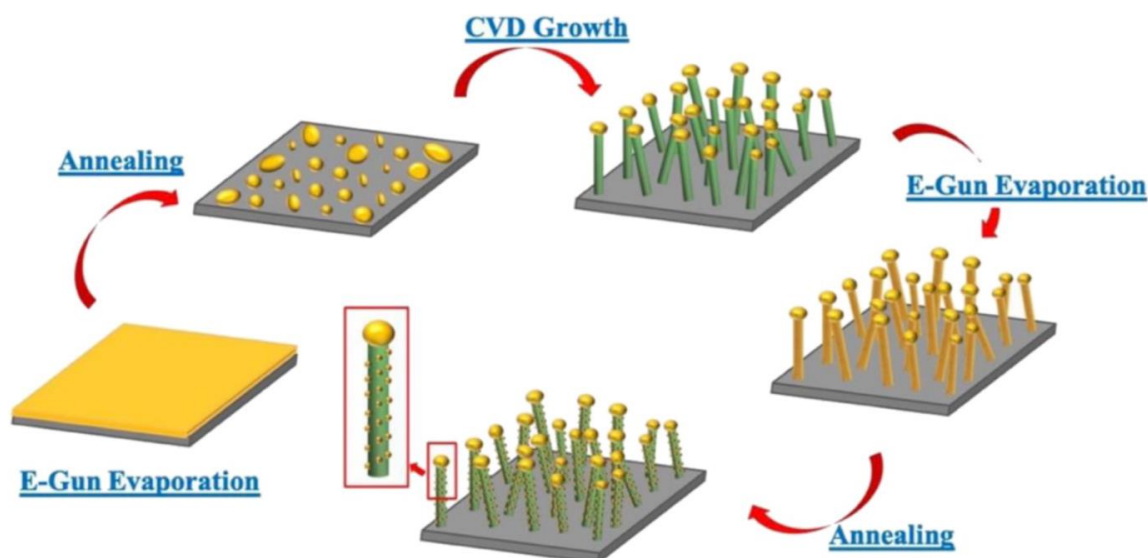
Figure 7. Schematic diagram of the fabrication of the Au NP/$Zn_xCd_{1-x}S$ NW heterostructure. Reproduced with permission from [75].

The pressure was maintained at 0.01 torr throughout the annealing process. Ternary $Zn_xCd_{1-x}S$ nanowires were synthesized by a simple one-step process. Before growth, commercial-grade ZnS powder (99.995%) CdS powder (99.999%), and a piece of Si (100) substrate coated with 10 nm of Au film as a catalyst were annealed. Argon flow was purged during the growth as a carrier gas and the pressure was maintained. After the heating process, the samples were cooled to room temperature in the furnace. The key factor in tuning the x ratio of the $Zn_xCd_{1-x}S$ nanowires was found to be temperature [75].

2.1.6. Sulfidation and Selenization

Figure 8a schematically illustrates the experimental setup used for the growth of WO_3 nanowires (NWs) as well as WS_2, WSe_2, and their ternary $WS_{2(1-x)}Se_{2x}$ nanotubes (NTs) on highly flexible carbon fibers (CFs) in a horizontal two-zone tube furnace [39]. High-density WO_3 NWs were used to cover the entire surfaces of the CFs vertically and uniformly, as shown in Figure 8c. The diameter and length of typical WO_3 NWs were found to be ca. 100 nm and the length was measured to be 5 μm. Then, the WS_2 and WSe_2 NTs were synthesized through sulfidization and selenization of WO_3 NWs at 800 °C, as demonstrated in Figure 8d,e.

For the synthesis of $WS_{2(1-x)}Se_{2x}$ NTs, the ratio of S and Se precursors were successfully altered for the controllable element component of ternary NTs (Figure 8f). As WO_3 NWs were used as a conversion template, the diameter and length of the WS_2 and WSe_2 NTs were found to be comparable to those of WO_3 NWs. Synthesis of the WS_2 NTs was conducted by the sulfidization of the WO_3 NWs performed at 800 °C in an Ar atmosphere. The chemical reaction is described as

$$2WO_3 + 7S \rightarrow 2WS_2 + 3SO_2$$
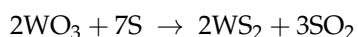
2.1.7. Successive Ionic Layer Adsorption and Reaction (SILAR) Method

The SILAR method is a simple, cost effective, and rapid technique for the deposition of binary semiconducting thin films when compared with other methods. It can be applied in the deposition of large-area thin films. Since this technique was introduced by Nicolau in the mid-1980s [76], this method has been employed to grow thin films, especially CdS, ZnS, and CdZnS. In particular, this method is appropriate for depositing thin films of chalcogenide groups I–VI, II–VI, III–VI, V–VI, VIII–VI binary, and I–III–VI, II–II–VI, II–III–VI, II–VI–VI and II–V–VI ternary chalcogenides and composite films. The SILAR method consists of the adsorption of the cation precursor, water rinsing, adsorption of the anion

precursor, followed by the appropriate reaction, and rinsing. These steps may be repeated. The schematic diagram illustrated in Figure 9 explains the mechanism of the SILAR growth.
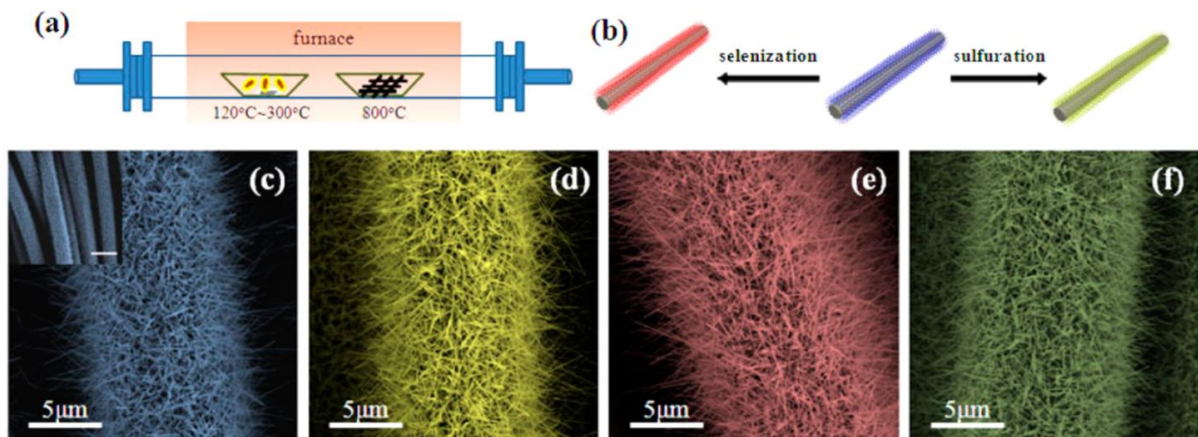

Figure 8. (**a**) Experimental setup of the preparation of WO_3 nanowires and WS_2, WSe_2, and $WS_{2(1-x)}Se_{2x}$ nanotubes. (**b**) Schematic diagram of WO_3 nanowires (NWs) converting to WS_2 and WSe_2 nanotubes (NTs) on carbon fibers by sulfidization and selenization. SEM images of (**c**) WO_3 NWs and (**d**) WS_2, (**e**) WSe_2, and (**f**) $WS_{2(1-x)}Se_{2x}$ NTs. Reproduced with permission from [39].
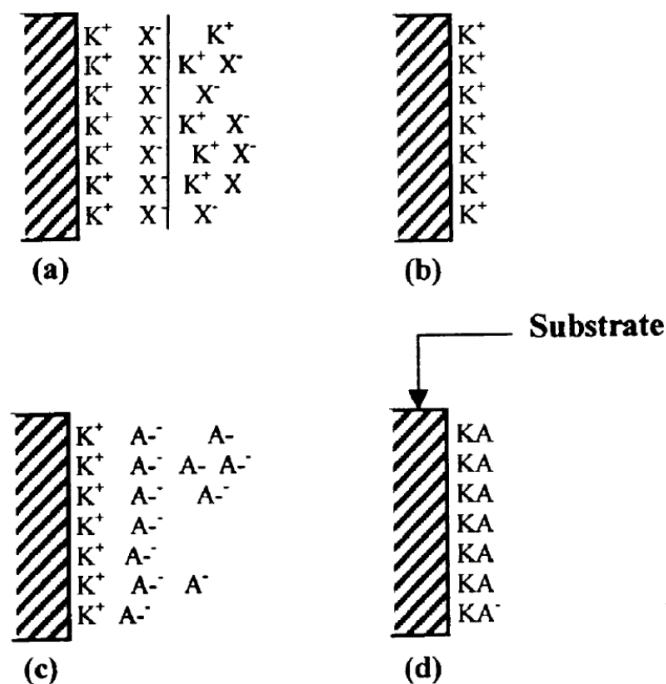

Figure 9. Schematic diagram of SILAR growth. (**a**) Adsorption of K^+X^- and the formation of electrical double layer, (**b**) first rinsing to remove excess, unabsorbed K^+ and X^-, (**c**) reaction of A^- with pre-adsorbed K^+ ions to form KA, and (**d**) second rinsing to remove excess and unreacted species and form the solid solution KA on the surface of the substrate. Reproduced with permission from [77].

In a typical process, the substrate is immersed separately in two precursor solutions and washed with water to remove the loosely bound species. By controlling the experimental conditions, the growth rates of thin films in the SILAR method can be varied between a quarter and a half of a monolayer [78–80]. Therefore, the aqua ligands remain at least partially intact during adsorption, thereby lowering the density of cations and anions in one layer. Furthermore, the growth of the thin film can be controlled at an accuracy of one SILAR cycle.

Valkonen et al. [80] studied the effect of different types of substrates by depositing ZnS, CdS films on glass, ITO-coated glass, and single crystals of GaAs (100). In this paper, they mainly focused on promoting interest in the SILAR method as applied to tin disulfide thin films. The authors used the SILAR method to prepare large-area ($\sim$10 cm^2) SnS$_2$ thin films on glass substrates under optimized deposition conditions. In addition, they reported SnS$_2$ thin films on a single crystal wafer of Si (111) to study the effect of substrate on the crystallinity of the films. In summary, these reports explain the feasibility of using the SILAR method for the preparation of TMC thin-films/coatings.

2.1.8. Refluxing Method

The refluxing method is a suitable method for the large-scale synthesis of TMCs such as SnS$_2$. In their paper, Liu et al. reported a facile refluxing method without using any templates or surfactants to synthesize SnS$_2$ nanocrystals with controllable morphology. It was found that the as-obtained SnS$_2$ nanostructures exhibited good adsorption ability and enhanced visible light photocatalytic activity for the degradation of Methylene Blue.

In a typical procedure, SnS$_2$ was prepared by using SnCl$_4 \cdot$5H$_2$O in the presence of ethylene glycol in a round bottom flask under stirring. The resultant mixture was heated to specific temperature followed by the addition of Na$_2$S solution under vigorous stirring. The resulting solution was refluxed under different temperature (120 °C and 180 °C) to obtain different samples.

In another study, Aditha et al. synthesized Cu$_2$ZnSnS$_4$ using the refluxing method. The experimental setup they used in their study is illustrated in Figure 10. A round bottom flask was fitted with a condenser connected to a water inlet and outlet to condense the vapor back into the reaction vessel to keep the total volume constant. In this method, the reaction temperature is the boiling point of the solvent in the reaction vessel [81].
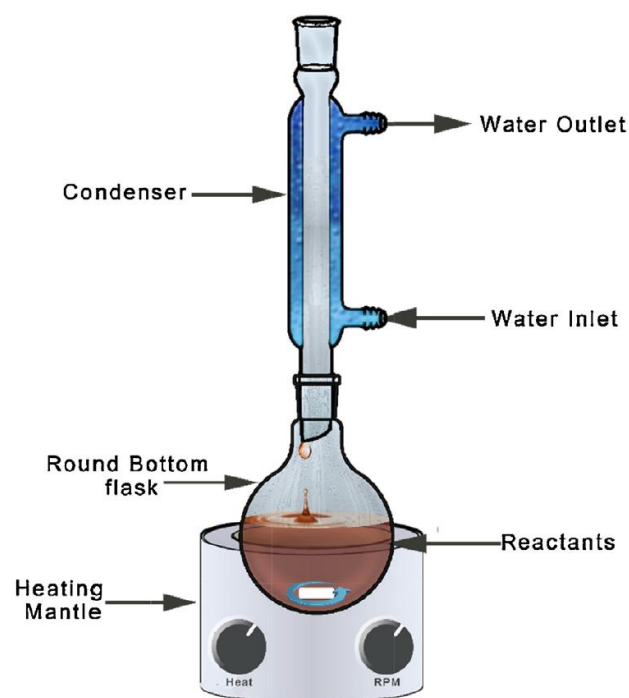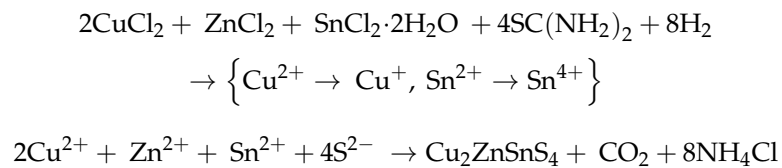

Figure 10. Schematic experimental setup of the refluxing method. Reproduced with permission from [81].

CuCl$_2$, ZnCl$_2$, SnCl$_2$·2H$_2$O, and thiourea were used as the precursor materials for producing Cu$_2$ZnSnS$_4$ and the refluxing time was 8 h. The reaction mechanism is given below.

$$2CuCl_2 + \ ZnCl_2 + \ SnCl_2·2H_2O \ + 4SC(NH_2)_2 + 8H_2$$

$$\rightarrow \left\{ Cu^{2+} \rightarrow \ Cu^+, \ Sn^{2+} \rightarrow Sn^{4+} \right\}$$

$$2Cu^{2+} + \ Zn^{2+} + \ Sn^{2+} + 4S^{2-} \ \rightarrow Cu_2ZnSnS_4 + \ CO_2 + 8NH_4Cl$$

Further to this, several other studies have also been performed by using the refluxing method to synthesize metal chalcogenide materials such as CuS [82], MoS$_2$ [83], ZnS [84], and NiS$_2$ [85].

2.1.9. Chemical Vapor Deposition (CVD) Method

A typical bottom-up method, the chemical vapor deposition (CVD) method, is the process during which gaseous or vapor materials react at a certain temperature in the gas phase or gas–solid interfaces to form solid products with low structural defects [44]. In the CVD method, parameters such as choice of the precursor, temperature, pressure, flow rate, time, the distance between precursor and substrate, and the choice of substrates influences the morphology, layer number, lateral size, orientation, and degree of defects [86–88]. Kwon et al. [89] provided a deep understanding of the thermodynamic and kinetic factors influencing the CVD method. Most importantly, the CVD method exhibits prominent advantages in controlling 2-D materials at an atomic-level, which allow for clarity of the structure–activity relationships.

Tan et al. utilized WS$_2$ materials with a graphene electrode for ultrathin 2-D photo detectors [90]. In another study, a 2-D-layered tin disulfide was synthesized by Chang et al. using the CVD method for photo detection of transistors by the thickness-controlled interface dynamics (TCID) technique, which shows high performance and great potential for several other applications [91].

Cong et al. synthesized single crystalline WS$_2$ monolayers by the direct sulfurization of WO$_3$ powders with sulfur powder at 750 °C; 300 nm using SiO$_2$/Si as the substrate. The substrate was covered with the WO$_3$ sample and another substrate was placed face down above it. After that, the setup (Figure 11) was heated in a small end closed quartz tube, which in turn was placed inside a big quartz tube using a tubular furnace [92].
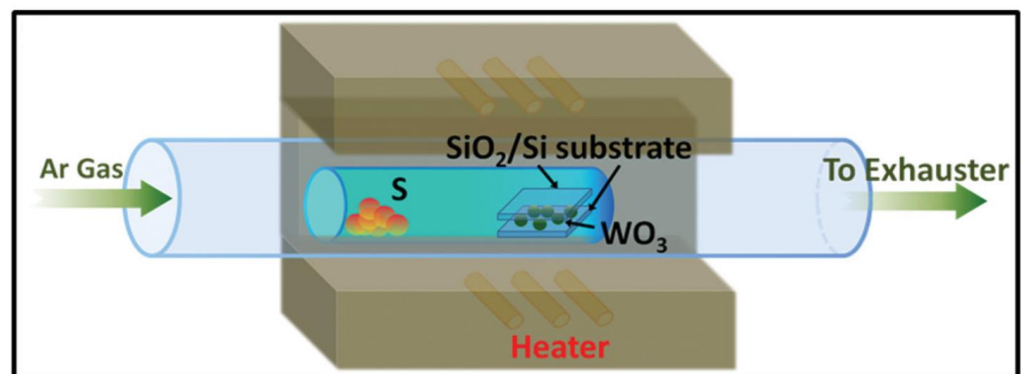
Figure 11. Schematic illustration of the chemical vapor deposition system used for the synthesis of WS$_2$. Reproduced with permission from [92].

In addition, SnS$_2$ [93], NiS [94], NiS$_2$ [94], MoS$_2$ [95], and FeS$_2$ [96] nanomaterials were also synthesized by using this CVD method in different studies.

2.1.10. Liquid Cascade Centrifugation (LCC) Method

In addition to the above-mentioned methods, synthesis of TMC can also be performed by a liquid cascade centrifugation (LCC) method to achieve a highly efficient nanosheet

with selected size and thickness [97]. LCC is an efficient, scalable, and versatile method that is based on a set of iterative centrifugation cascades designed to achieve highly efficient nanosheets and/or monolayer enriched dispersions. Mihai et al. synthesized liquid-exfoliated 2D WS_2 and MoS_2 nanosheets by the liquid centrifugation cascade method and the prepared nanosheets were used for neuromorphic computing applications [98]. Figure 12 illustrates the LCC method used in their study to separate the nanosheets efficiently according to their size and thickness.
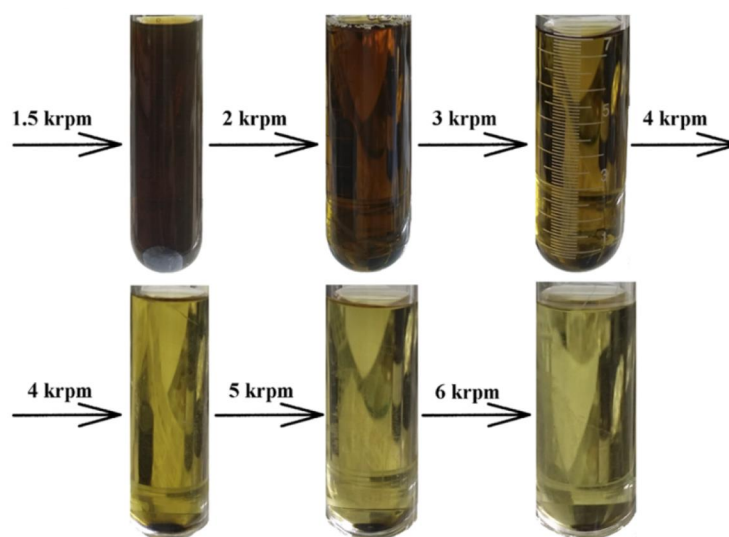

Figure 12. The LCC method used to separate the nanosheets. Reproduced with permission from [98].

The following Table 1 discusses the different synthesis methods used in the preparation of TMC nanoparticles and the specific advantage(s)/disadvantage(s).

Table 1. Summary of the different types of the synthesis method of TMC.

Synthesis Methods	Advantages/Disadvantages
Hydrothermal/Solvothermal Method	Produce nanomaterials with various morphologies and thicknesses at high pressure and low temperature; can synthesize high quality large crystals; cost of equipment is high
Microwave-assisted Synthesis	Required less time/rapid process; size can be controlled
Electrodeposition Method	Rapid and single-step process; used to produce homogeneous and high-purity crystalline materials at the cathode of the electrochemical system during the coating process
Photoreduction	Require higher photon energy; can synthesize the materials with large surface area and many active sites
Electron Beam Evaporation	0D, 1D, and 2D materials can be prepared; used for depositing materials with high melting point; as electrons can be focalized, it is possible to obtain a very localized heating on the material to evaporate with a high density of evaporation power
Sulfidation and Selenization	Solution-phase conversion; facile and selectable synthesis method
Successive Ionic Layer Adsorption and Reaction (SILAR) Method	Simple, cost effective, and rapid technique for the deposition of binary semiconducting thin films
Refluxing Method	Large scale synthesis method; facile and cost effective
Chemical Vapor Deposition (CVD) Method	Gas-phase aerosol process for producing high-purity nanoparticles; mainly used for large scale thin-film production
Liquid cascade centrifugation (LCC) method	Used to achieve highly efficient nanosheet with selected size and thickness; most efficient, scalable, and versatile method based on a set of iterative centrifugation cascades

2.2. Characterization Techniques

There have been various techniques such as X-ray diffraction spectroscopy (XRD), scanning electron microscopy (SEM), UV–Visible spectroscopy/diffuse reflectance spec-

troscopy (UV-DRS), and X-ray photoelectron spectroscopy (XPS) used to characterize the transition metal chalcogenides, which are discussed in the following section.

2.2.1. X-ray Diffraction Method (XRD)

X-ray diffraction method is a non-disruptive technique used to characterize the crystallite size, crystallinity, crystal structure, and phase composition of the material in a powder or film.

Figure 13 shows the XRD patterns of SnS_2 nanosheets (NSs) that confirm the formation of 2T-type hexagonal SnS_2 NSs (space group P$\bar{3}$m1) with cell parameters of a = b = 3.649 Å and c = 5.899 Å. A high crystalline and pure product was obtained when compared with the standard diffraction data of JCPDS no. 23-0677. The highest intensity peak was assigned to the (001) facet of the indicating hexagonal phase [38]. Figure 14 shows the XRD patterns for MoS_2 and WS_2 on carbon cloth at different thermolysis temperatures. The peaks at 26.8° and 43.5° (marked as "C") can be ascribed to the carbon cloth in all samples. As shown in Figure 14a, the presence of the (002) reflection peak at 2θ = 14.2° indexed the periodicity along the direction perpendicular to the planar structure of MoS_2. This was only observed for the MoS_2 samples heated at 1000 °C, but not at lower temperatures. For the WS_2 samples, peaks were observed at lower temperatures (i.e., 200 and 400 °C). As the thermolysis temperature increased, higher crystallinity of WS_2 was observed. For WS_2 samples prepared at 800 and 1000 °C, the reflection peak was found for WO_3, which is marked with * in Figure 14b.

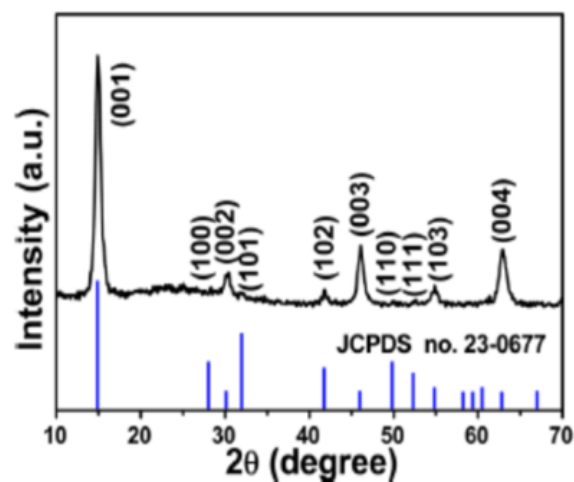**Figure 13.** XRD pattern of SnS_2 nanosheets (NSs) prepared at 220 °C for 12 h. Reproduced with permission from [38].
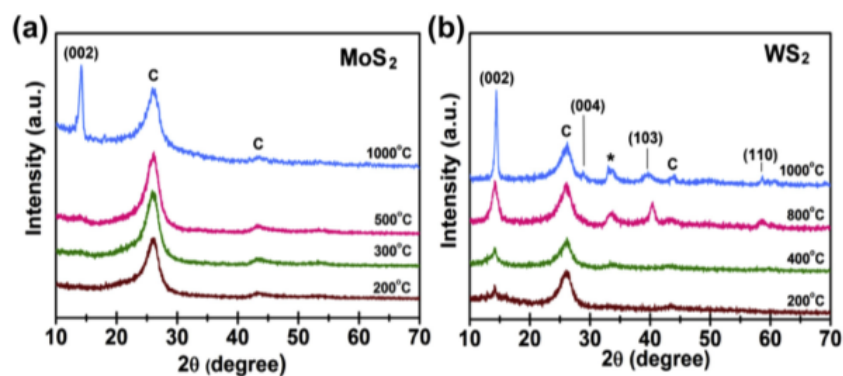

Figure 14. XRD pattern for the samples obtained at different thermolysis temperatures: (**a**) MoS_2 on carbon cloth and (**b**) WS_2 on carbon cloth. Peaks with notation C represent the carbon peaks from carbon cloth. (*) indicates the peaks from WO_3. Reproduced with permission from [99].

Figure 15 shows the XRD patterns indexed to g-C$_3$N$_4$ for different heating times and MoS$_2$ samples. The bottom (green) XRD pattern was indexed to a hexagonal phase of MoS$_2$ (JCPDS 37-1492) [100]. The peaks observed at 2θ = 32.6° and 58.3° corresponded to the (100) and (110) crystal planes of metal chalcogenide, respectively. In addition, the XRD patterns of CN2.5, CN10, and CN20 samples showed similar peaks, as indicated in Figure 15 (JCPDS 87-1526). The peak at 2θ = 27.4° was indexed to the (002) stacking layered structure of g-C$_3$N$_4$ and the 2θ = 13.0° peak corresponded to the (100) in-plane of the repeating units [101]. The CM0.05 heterostructure pattern showed the sole g-C$_3$N$_4$ peaks without the MoS$_2$ peaks due to the low content of MoS$_2$ [102–104].
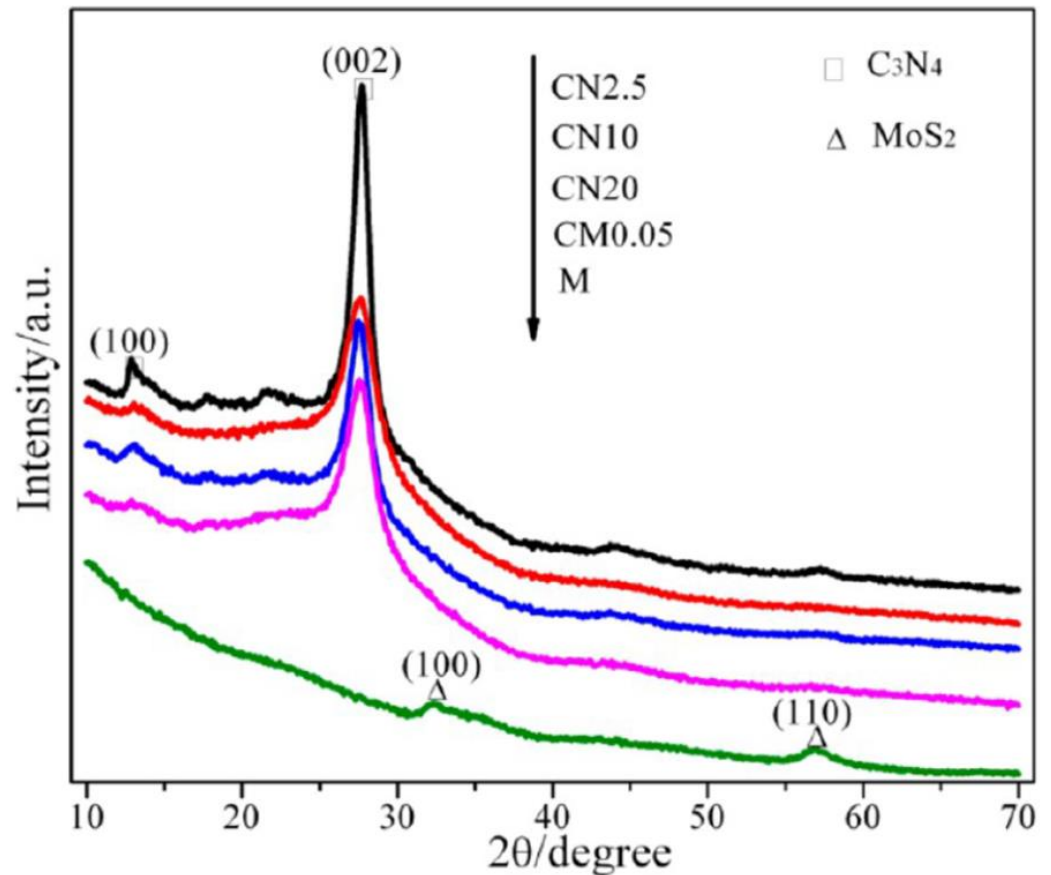
Figure 15. XRD patterns of CN2.5, CN10, CN20, CM0.05, and M (MoS$_2$). Reproduced with permission from [101].

In a different study, pure CoS$_2$, pure TiO$_2$, and 10 wt. % CoS$_2$/TiO$_2$ were successfully synthesized using the hydrothermal method [105]. XRD patterns confirmed the formation of these nanoparticles and the Figure 16 demonstrates the structural quality and phase orientation of the synthesized nanocomposite between the 2θ = 20° and 70° diffraction angles. The XRD confirmed the anatase phase formation for TiO$_2$, whereas the CoS$_2$ phase formation was confirmed by the appearance of peaks at the 2θ degrees of 26.04°, 31.58°, 37.08°, 40.34°, 45.34°, and 55.1° for the (111), (200), (210), (211), (220), and (311) diffraction planes, respectively (JCPDS Card No.: 9007682). Impregnation of CoS$_2$ on TiO$_2$ was confirmed by the combined XRD peaks obtained with the 10 wt. % of CoS$_2$/TiO$_2$ nanocomposite materials.
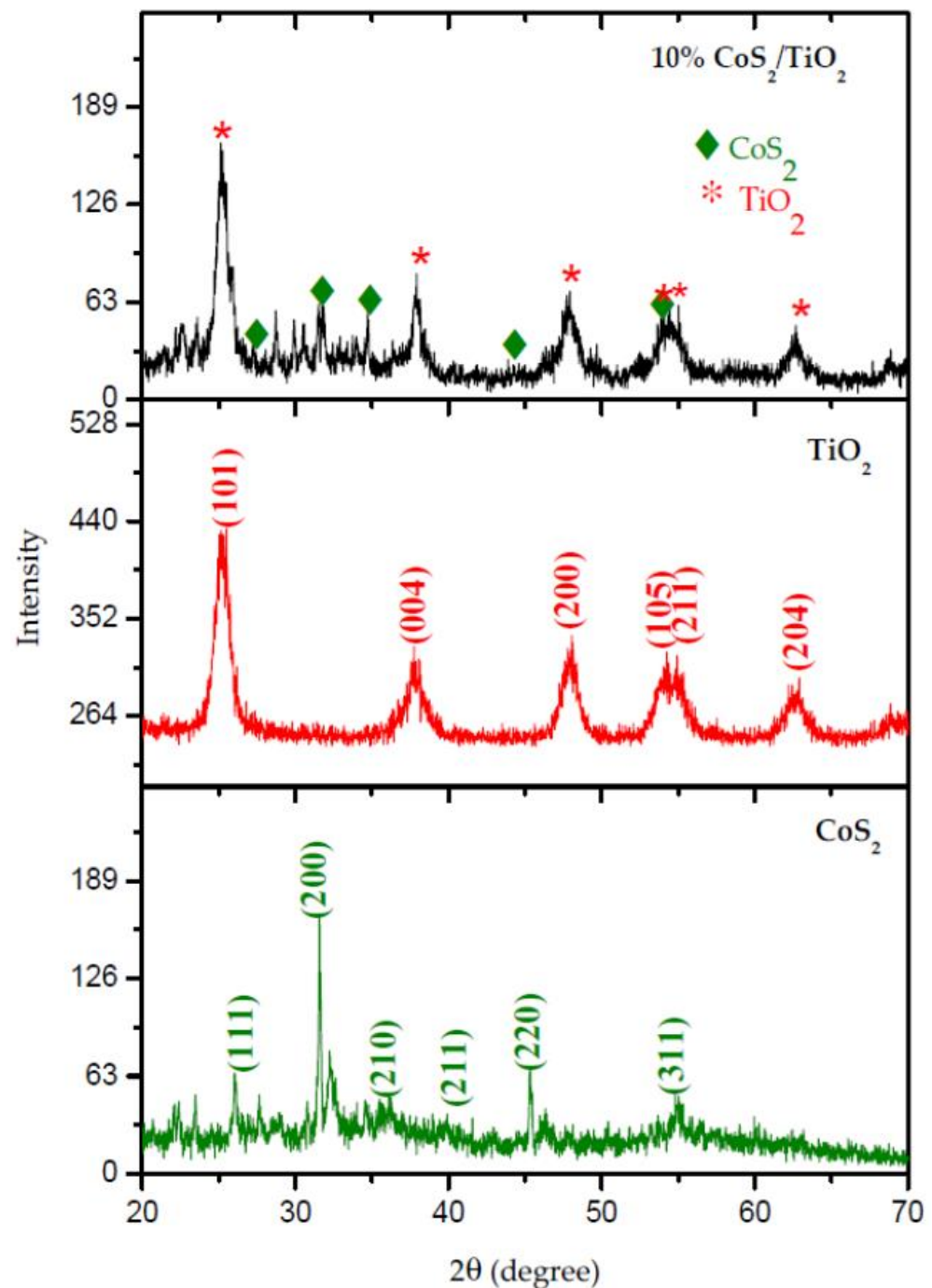
Figure 16. XRD pattern of pure CoS_2, pure TiO_2, and 10 wt. % of the CoS_2/TiO_2 nanocomposite. Reproduced with permission from [105].

In another study, SnS_2/TiO_2 nanocomposites were synthesized by the hydrothermal method, and XRD analysis was carried out to characterize those materials. Figure 17 shows that the peaks at the 2-theta value of 25.29, 37.88, 48.25, 53.74, 55.14, 62.71, 68.86, 70.30, and 75.06 for the pure TiO_2 nanoparticles were due to the (101), (004), (200), (105), (211), (204), (116), (220), and (215) diffraction planes of the anatase phase of TiO_2, which was well matched with the JCPDS:00-004-0477. The observed peaks at 2θ values of 14.76, 27.97, 32.00, 41.79, 49.92, 52.41, 54.79, and 60.55 for pure SnS_2 was correlated to the (001), (100), (101), (102), (110), (111), (103), and (201) diffraction planes (JCPDS:00-023-0677).

Combined peaks of both SnS_2 and TiO_2 were observed with the 5, 10, 15, and 20 wt. % SnS_2/TiO_2 (ST-5, ST-10, ST-15, and ST-20, respectively) nanocomposite and confirmed the good impregnation of SnS_2 on TiO_2 in their study [106].

2.2.2. Scanning Electron Microscopy (SEM)

Scanning electron microscopy (SEM) is an established technique used to analyze the morphology of the sample, especially given the simplicity of the sample preparation. Estimates of the sample composition can be obtained through energy dispersive X-ray spectroscopy (EDS).
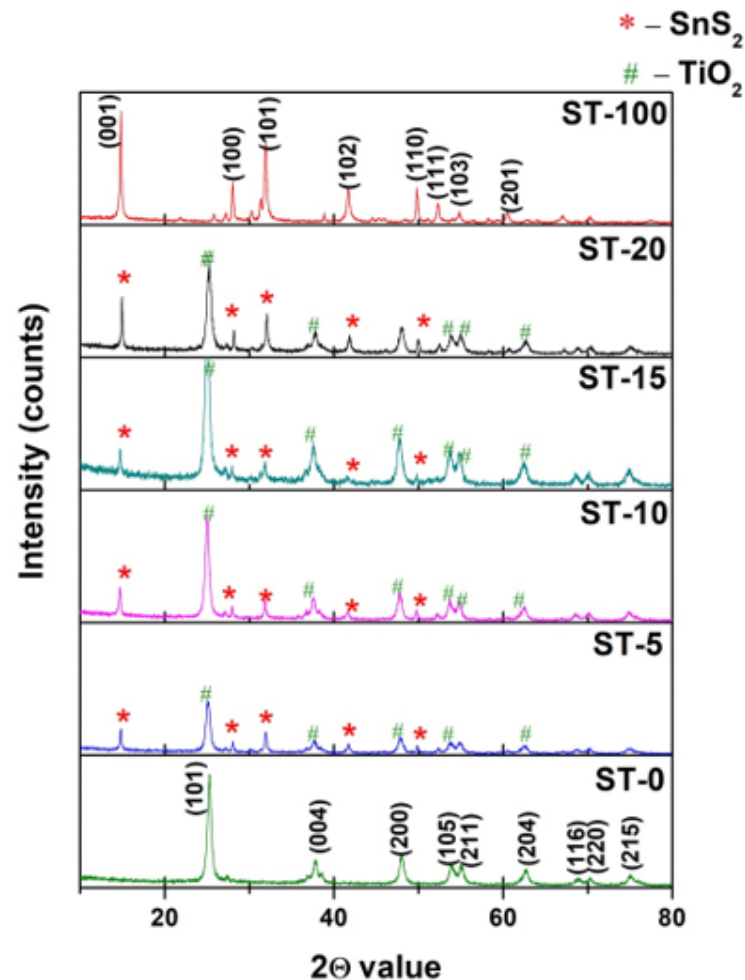
Figure 17. XRD image for pure SnS_2 (ST-100), pure TiO_2 (ST-0), different wt. % of SnS_2/TiO_2 materials 5% (ST-5), 10% (ST-10), 15% (ST-15), and 20% (ST-20). Reproduced with permission from [106].

In addition, the particle size distribution can also be easily obtained with relative ease, and thus, many of the reported works have used this simple characterization technique to study the TMC materials using SEM.

Figure 18 exhibits the phase and morphology transformation of intermediates during the formation of monodispersed SnS_2 nanosheets; consequently, the effects of the reaction parameters including reaction time and the dosage of polyvinylpyrrolidone (PVP) on the morphology of SnS_2 was also studied. PVP was used as a steric stabilizer or capping agent to minimize aggregation of the colloidal particles.

Figure 18. SEM images of the SnS$_2$ samples prepared at different reaction times. (**a**) 1 h; (**b**,**c**) 2 h; (**d**) 5 h; (**e**) 12 h; and (**f**) 24 h. Reproduced with permission from [38].

Figure 18a shows the structure of orthorhombic SnS microspheres stacked by sheets, which were first nucleated in the primary stage of a chemical reaction. When the reaction time increased to 2 h, small sheets expanded and grew onto larger sheets. At the same time, in Figure 18b, the spherical flower-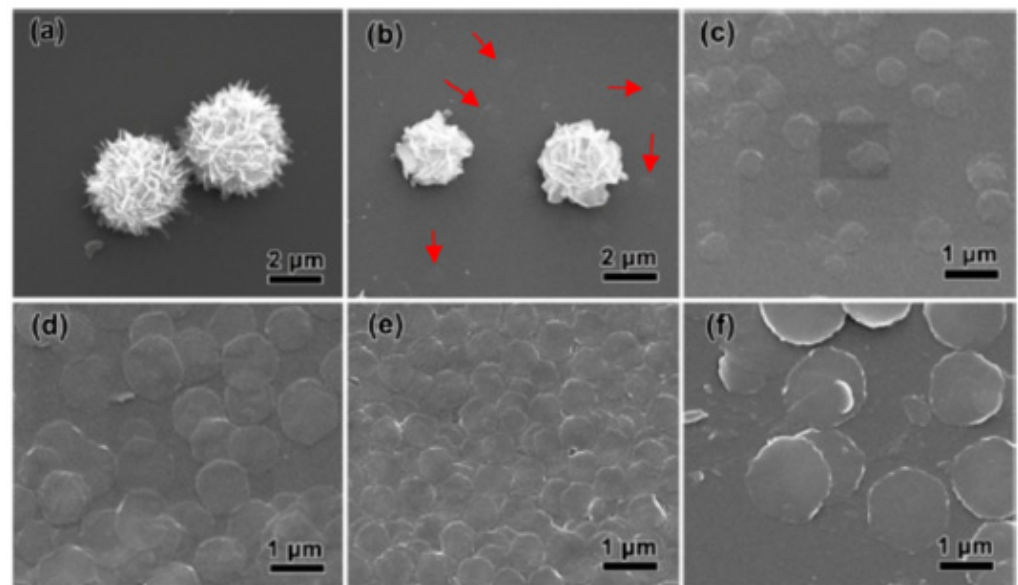like morphology remained and the regular nanosheets were deposited around micro-flowers. Figure 18c is the high-magnification SEM image with the reaction time of 2 h, which exhibits the deposited nanosheets. When the reaction time was prolonged to 5 h, uniform nanosheets were obtained with the single phase of hexagonal SnS$_2$. Consequently, it was proven that the SnS phase would be oxidized into SnS$_2$ gradually as the reaction progresses. Furthermore, as the reaction time increases, SnS$_2$ nanosheets tend to grow and enhance their crystallinity [38], which was proven by SEM analysis.

In another study, a different TMC, NiS$_2$ particles with a hollow structure, were synthesized and characterized by FESEM. Figure 19a,b indicates the FESEM images of NiS$_2$ hollow microspheres prepared on a large scale. Figure 19b shows that the diameter of NiS$_2$ hollow microspheres was about 3 μm and it was found that the surface of the microspheres was rough. The thickness of the wall was found to be approximately 200 nm (Figure 19c), and the hollow structure can be clearly seen in this image. Figure 20d shows a high-resolution TEM image that displays the lattice fringes of NiS$_2$. The lattice distance was 0.286 nm, which corresponds to the (200) crystal plane [13].

In a different study, TMC doped TiO$_2$ materials were synthesized and studied for hydrogen production. Sivagowri et al. synthesized a CoS$_2$/TiO$_2$ nanocomposite using hydrothermal methods. As shown in the SEM images of pure CoS$_2$ (Figure 20a,b), aggregates stacked by flake-like structures were attained. The image for pure TiO$_2$ (Figure 20c,d) showed an irregular 3-D block-like structure covered with spongy like particles, whereas CoS$_2$/TiO$_2$ indicates a hexagonal rod like structure decorated with sponge like materials, as illustrated in Figure 20e,f [105].
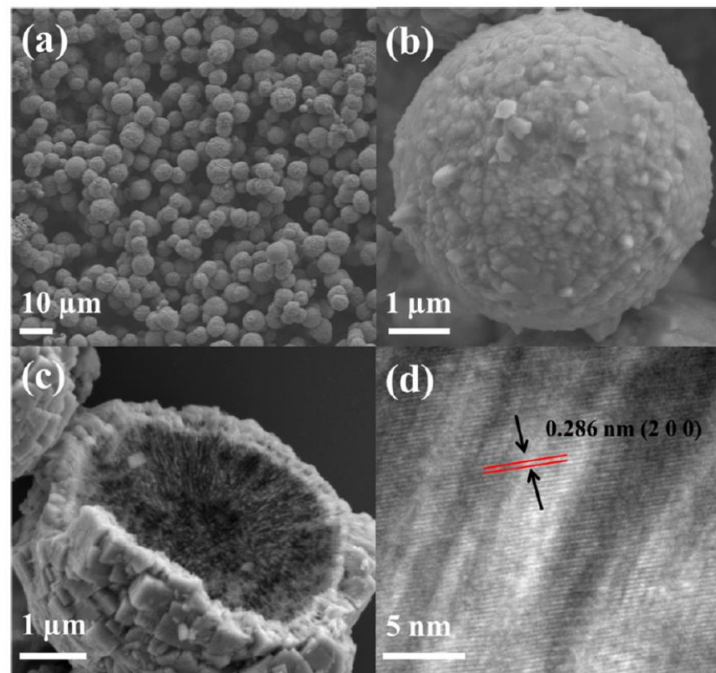
Figure 19. (**a**–**c**) Field emission scanning electron microscopy (FESEM) images of NiS$_2$ hollow microspheres at different magnifications. (**d**) High-resolution transmission electron microscope (TEM) image of NiS$_2$. Reproduced with permission from [13].
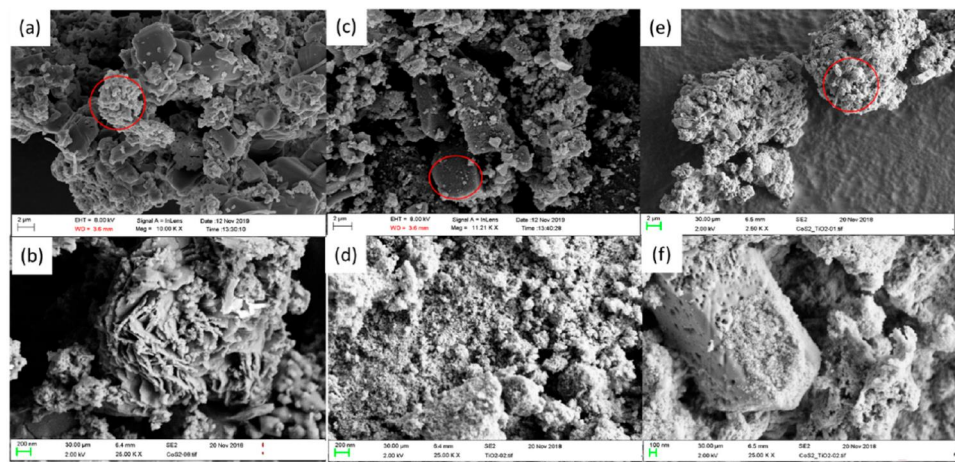
Figure 20. SEM images of (**a**,**b**)—pure CoS$_2$, (**c**,**d**)—pure TiO$_2$, and (**e**,**f**)—CoS$_2$/TiO$_2$ nanocomposites. Reproduced with permission from [105].

The same group, in a different study, reported that a different morphology was attained with SnS$_2$–TiO$_2$ nanocomposites when only the TMC was changed. In the SEM study, they observed that the pure TiO$_2$ nanoparticle showed an irregular 3-D block-like structure covered with sponge-like particles as indicated in Figure 21a. The micrograph obtained in the higher magnification (Figure 21b) image indicates that the aggregated particles had spongy-like structures. A flower-like structure composed with nanosheets was attained for pristine SnS$_2$ and is shown in Figure 21c,d.
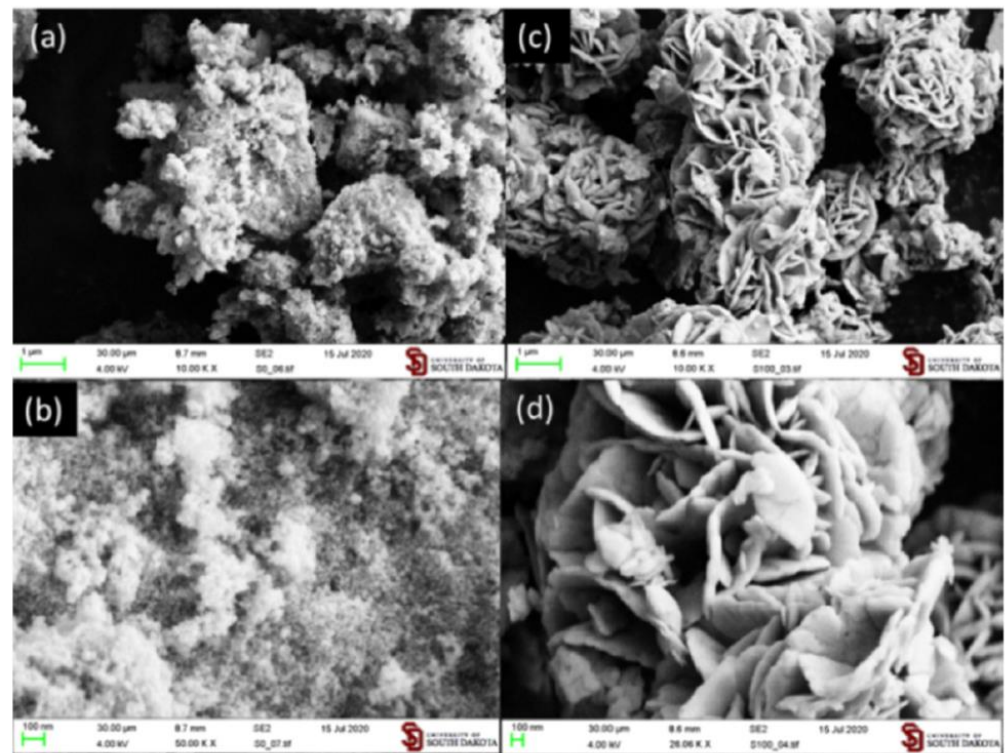
Figure 21. SEM images for (**a**,**b**)—pure TiO$_2$ and (**c**,**d**)—pure SnS$_2$. Reproduced with permission from [106].

The SEM images of different wt. % of SnS$_2$ that included 5% (Figure 22e), 10% (Figure 22f), 15% (Figure 22g), and 20% (Figure 22h) embedded TiO$_2$ nanocomposites are shown in Figure 22. The surface morphology of these SnS$_2$/TiO$_2$ nanocomposites at different wt. % possessed nanosheets, and it can be seen that the sponge-like materials covered the structure and, therefore, exhibited significant aggregation [106].
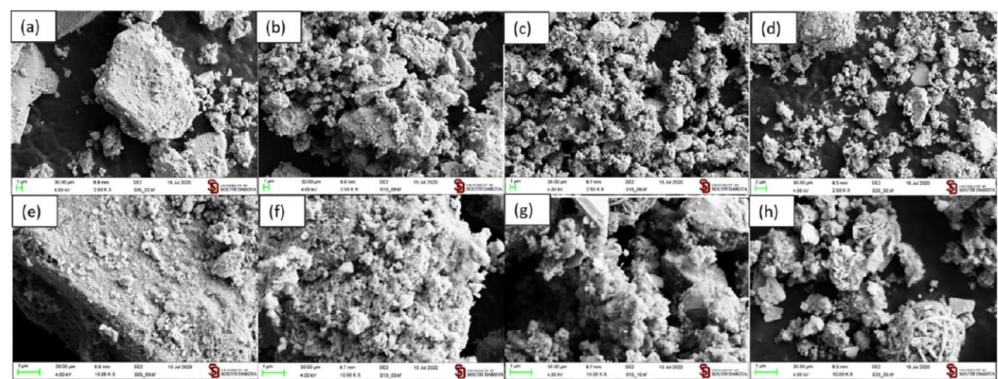
Figure 22. SEM images for different wt. % of SnS$_2$/TiO$_2$ (**a**,**e**) 5%, (**b**,**f**) 10%, (**c**,**g**) 15%, and (**d**,**h**) 20%. nanocomposites. Reproduced with permission from [106].

2.2.3. X-ray Photoelectron Spectroscopy (XPS) Studies

X-ray photoelectron spectroscopy (XPS) is based on the photoelectric effect and was used to investigate the chemical state and surface elemental composition of the samples. Among the literature collected, it was found that only a few reports have presented the XPS analysis of TMC material, which may be due to the necessity of the analysis for the structure–activity correlation. In a study by Bo Gao et al., a MoS$_2$/candle soot composite was synthesized and analyzed using XPS. Figure 23 shows the existence of the elements C, Mo, and S with a small amount of O. The corresponding peaks indicate the binding

energies at 284.6 (C 1s), 161.5 (S 2p), 231.0 (Mo 3d), and 529.1 eV (O 1s), respectively. In addition, the atomic ratio between Mo and S was found to be 0.43. Figure 23b illustrates the presence of peaks with binding energies of 232.8 and 229.7 eV, which may be ascribed to Mo $3d_{3/2}$ and $3d_{5/2}$ of 2H-MoS$_2$ at the peaks at 228.9 eV for $3d_{5/2}$, and at 231.9 eV for $3d_{3/2}$, which was ascribed to 1T-MoS$_2$ [107]. The peak located at 226.9 eV corresponded to the binding energy of S 2s. In addition, the two weak peaks at 233.6 and 236.1 eV were due to the presence of the MoO$_3$ that formed during the sputtering process. From these results, they found that Mo^{4+} dominates the product. Similarly, the two doublet peaks located at 162.6 eV and 164.1 eV corresponded to the $2p_{3/2}$ and $2p_{1/2}$ orbitals of 2H-MoS$_2$. Furthermore, the binding energies at 161.6 eV and 163.2 eV were due to 1TMoS$_2$. The high-resolution spectra of XPS further provides evidence for the existence of MoS$_2$ in the hybridized samples [108].

In a different study, Li and coworkers used XPS characterization to study the Pt doped CdS materials and Figure 24a illustrates the XPS spectrum of the Pt–CdS, indicating the co-existence of Cd, S, and Pt elements in the as-prepared Pt–CdS composite. The peaks at 405.6 and 412.3 eV corresponded to the Cd $3d_{5/2}$ and Cd $3d_{3/2}$ of CdS, respectively (Figure 24b) [25]. In Figure 24c, the S $2p_{1/2}$ and S $2p_{3/2}$ peaks are located at 163.2 and 161.9 eV, respectively.

2.2.4. UV–Visible Spectroscopy/Diffuse Reflectance Spectroscopy (DRS)

Like all nanomaterials, to study the bandgap and the optical behavior of the TMCs, researchers have utilized UV–Visible diffuse reflectance spectroscopy. In this regard, in the study of the facile hydrothermal synthesis of a 3-D flower-like La-MoS$_2$ nanostructure for photocatalytic hydrogen energy production, Riaz et al. utilized this technique to study the bandgap of La doped MoS$_2$ materials, as illustrated in Figure 25.
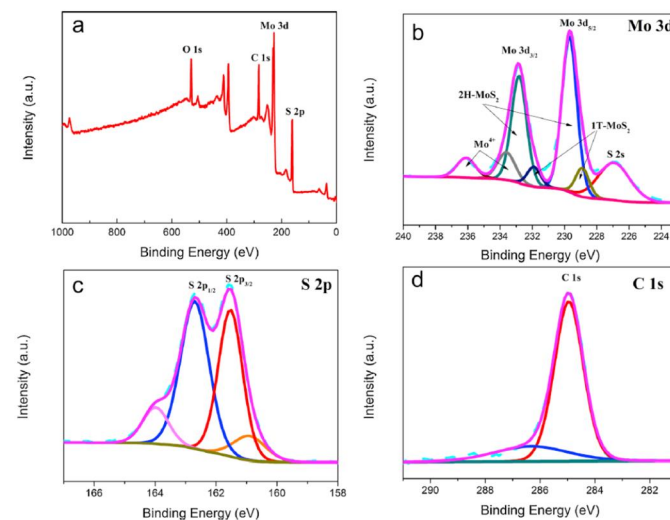
Figure 23. Full XPS spectra of (**a**) MoS$_2$/candle soot composite, (**b**–**d**) high-resolution XPS spectra of Mo 3d, S 2p, and C 1s for MoS$_2$/candle soot composite. Reproduced with permission from [108].
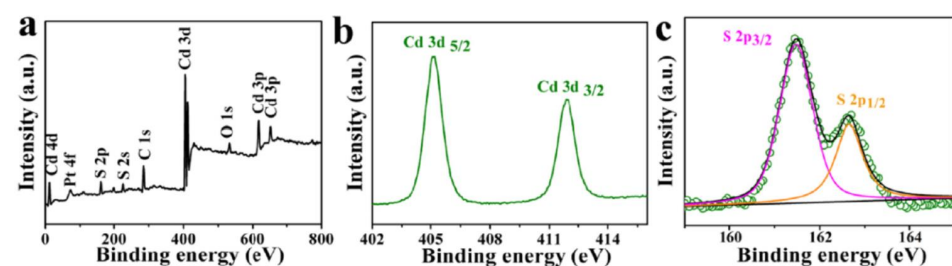
Figure 24. (**a**) XPS of Pt-CdS and the corresponding high-resolution XPS spectra of Pt–CdS, (**b**) Cd 3d, and (**c**) S 2p. Reproduced with permission from [25].
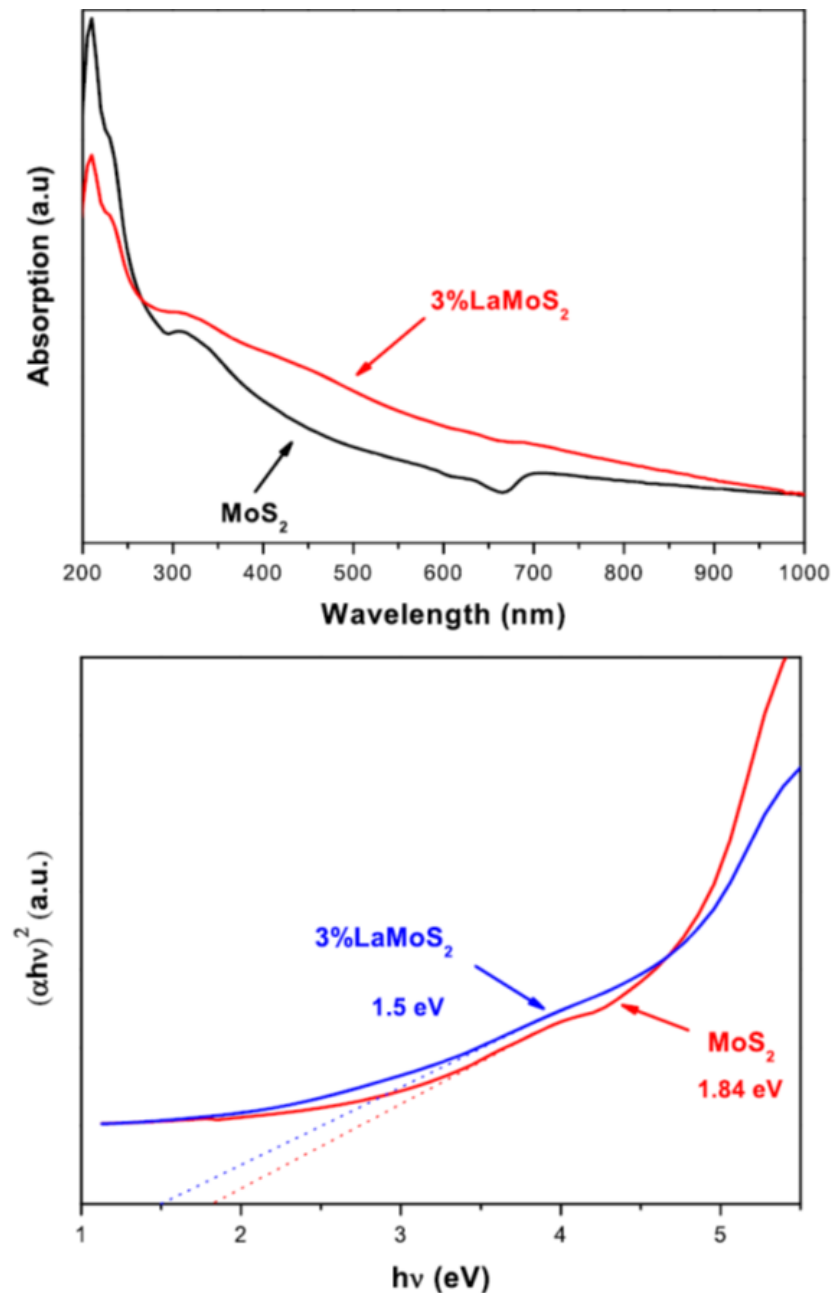
Figure 25. UV–Visible absorption spectra of 3-D flower-like MoS_2 and 3% $LaMoS_2$ nanoflake samples. Reproduced with permission from [109].

The absorption spectra of pure MoS_2 and 3% La-MoS_2 indicate that the absorption of $LaMoS_2$ was significantly extended toward a longer wavelength than pure MoS_2 into the visible light range. Bandgap energy for pure MoS_2 calculated by using the equation $(\alpha h\upsilon)^2 = A(h\upsilon - Eg)$ allowed for direct transitions, resulting in a value of 1.84 eV, which is illustrated in the plot of $(\alpha h\upsilon)^2$ vs. $h\upsilon$ (eV) (Figure 25). This value is close to the bandgap energy of 1.8 eV for a monolayer of MoS_2 [110]. However, 3% La-MoS_2 showed a considerably small bandgap energy of 1.5 eV due to La^{3+} doping, which significantly improved the light absorption properties of MoS_2 [109].

Gaur et al. used SnS_2 nanoparticles as photocatalysts for the reduction of Cr(VI) and their optical properties were investigated by DRS studies. Figure 26a,b shows DRS and Tauc plots of SnS_2 nanoparticles. Bandgap absorption in the range between 430 nm and 580 nm was observed. The bandgap calculated by using the Tauc plot indicates values between 2.31 eV and 2.94 eV [111].

In addition to these methods, Raman spectroscopic technique and photoluminescence studies (PL) were also utilized to analyze these TMC materials. However, there is a limited number of literature available, especially with the PL and AFM studies on the TMC materials toward hydrogen production application, and thus, were omitted in this review.

2.2.5. Raman Spectroscopy

L. Zhu et al. synthesized CoS_2-based thin films as model catalysts for the oxygen reduction reaction, which were characterized by using Raman spectroscopy. Figure 27 shows characteristic peaks at 287 and 389 cm^{-1} as well as a shoulder around 410 cm^{-1} for the CoS_2 powder. This was in close agreement with the study of a CoS_2 single crystal [112]. The peak at 287 cm^{-1} was also associated with polysulfides. In contrast, the Raman spectrum obtained from the magnetron-sputtered thin film of CoS_2 showed a pronounced peak at 391 cm^{-1}, a broad shoulder at around 410 cm^{-1}, and another peak at 287 cm^{-1}, which exhibited a general similarity to the spectrum obtained for the standard CoS_2. Furthermore, the Raman spectrum of commercial NiS_2 was also reported in their study and it showed distinctive peaks at 282 and 477 cm^{-1}, and a shoulder at 488 cm^{-1} (Figure 27). From this study, they confirmed the formation of CoS_2 with the expected characteristics.
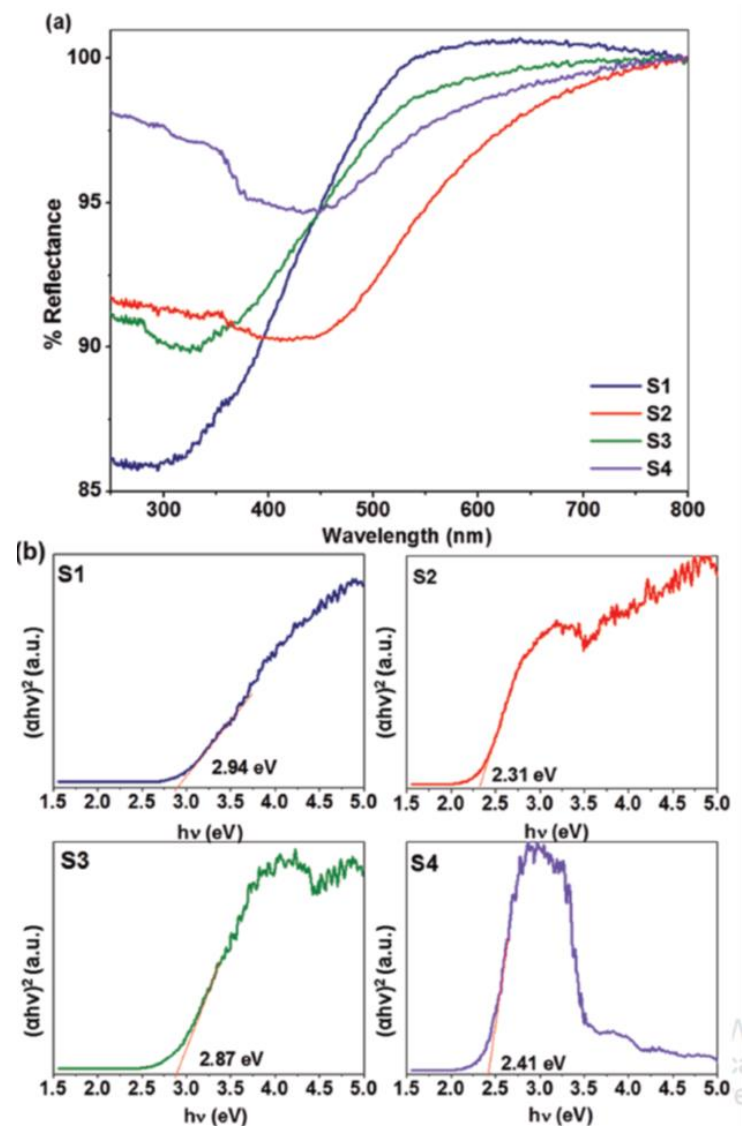

Figure 26. (**a**) DRS spectra and (**b**) Tauc plots for SnS_2 nanoparticles synthesized by using different reactants and solvents. Reproduced with permission from [111].
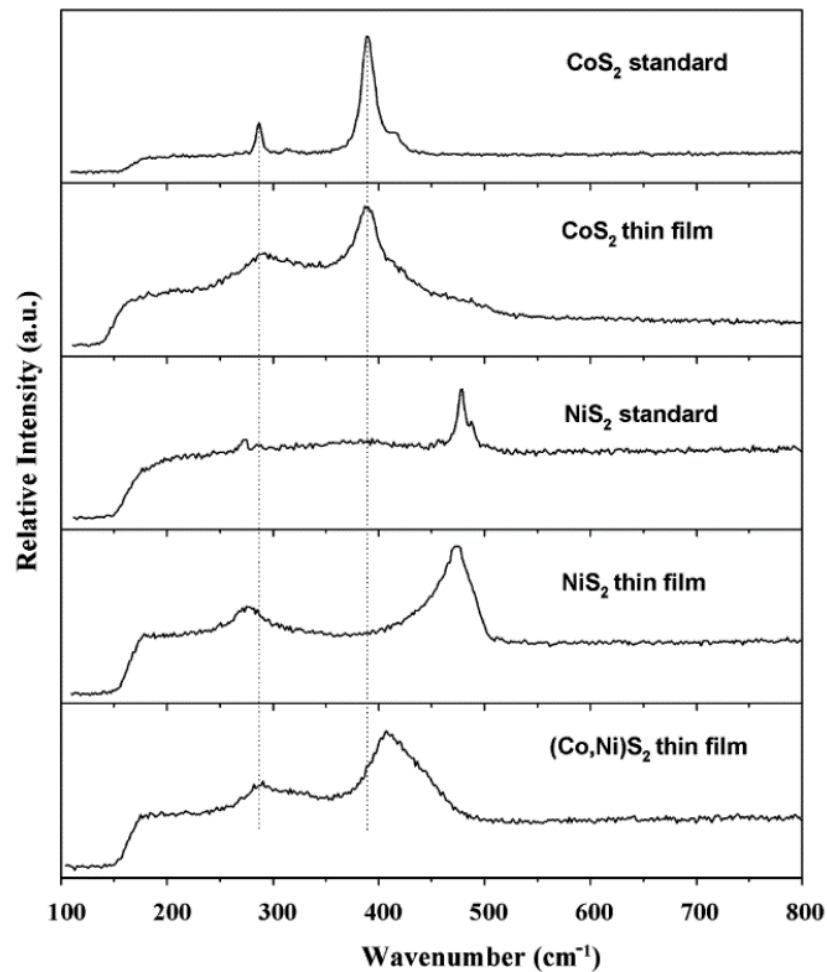
Figure 27. Raman spectra measured with HeNe laser for the CoS_2, NiS_2 and $(Co,Ni)S_2$ thin films and compared with those measured for standard CoS_2 and NiS_2 samples. Reproduced with permission from [112].

3. Hydrogen Evolution Reactions

Production of hydrogen through water splitting is seen as an extremely important renewable and clean energy [4]. Since water is abundant, and as novel materials are synthesized and the technology of water splitting becomes mature, hydrogen can be produced from water by different methods such as thermolysis (e.g., thermochemical cycles), electrolysis (e.g., electrocatalysis), photolysis (e.g., photocatalysis), and biolysis (e.g., dark fermentation) [113].

Among them, electrolysis of water, which includes the cathodic hydrogen evolution reaction (HER) [113] and anodic oxygen evolution reaction (OER) [113], remains limited by the high cost of noble metals such as Pt [114] and Ru [115] based materials, which are typically used as electrocatalysts in different electrolyte materials that include acid and base electrolytes [116]. In addition, different photocatalytic materials are being used to utilize solar energy for splitting water [37,105,117]. Photoelectrochemical and photocatalytic are the two main methods for water splitting. In the photoelectrochemical method, a semiconductor photoelectrode is typically used as the working electrode and is immersed in an aqueous electrolyte. A counter and reference electrode are used to complete the cell. An electrochemical potential is then applied to the photoelectrode. A light source is used to excite the semiconductor electrode. If an n-type semiconductor is used, the photoexcited electrons generated in the photoanode travel to the counter electrode (via an external wire) and reduce protons to form hydrogen. At the working electrode, the holes oxidize water to

produce oxygen and an anodic photocurrent is produced. Thus, the products, hydrogen and oxygen, are produced at separate electrodes.

In the photocatalytic method, the semiconductor powder is suspended in water. The slurry is irradiated by an appropriate light source. Bandgap excitation leads to the generation of electrons and holes. These charge carriers migrate to the surface and dissipate their charges and produce hydrogen and oxygen, respectively. In photocatalysis, the product separation is required. Nowadays, researchers are putting great effort into maximizing the production of hydrogen by water splitting with the eventual aim to generate hydrogen through sustainable ways [13,118–120].

The following table (Table 2) lists the different hydrogen production methods and their advantages and disadvantages.

Table 2. Different hydrogen production methods and its advantages and disadvantages.

Hydrogen Production Methods	Description	Advantages	Disadvantages	Reference
Steam natural gas reforming	Direct production of hydrogen gas by conversion of feed hydrocarbons at high temperature	• Most viable technology to begin building hydrogen market • Existing feedstock infrastructure	• Capital investment is high • High operation and maintenance expenses • CO_2 byproduct • Dependence on fossil fuels	[121–123]
Coal gasification	Partial oxidation of coal with air. However, it generates the CO_2 through traditional combustion	• Low-cost • Uses abundant and affordable coal feedstock	• High reactor costs • System efficiency • Feedstock impurities • Carbon capture and storage	[123,124]
Biomass gasification	Burning of biomass using limited supply of air generates combustible gases, such as CO, CO_2, H_2 CH_4, H_2O and N_2 with contaminants like small char particles, ash and tars	• CO_2-neutral, abundant and cheap feedstock	• Tar formation • Varying H_2 content due to seasonal • Availability and feed stock impurities	[122,125]
Thermolysis	Using high temperature from concentrated solar energy and chemical reactions to generate the H_2 and O_2 from water.	• Clean and Sustainable, abundant feedstock • O_2 is the only byproduct; No greenhouse gas emissions	• Element's toxicity • Corrosive problems • High capital costs	[122,123]
Electrolysis	Usage of electricity to split water into hydrogen and oxygen	• Emission-free, proven technology, existing infrastructure • Abundant feedstock • O_2 is the only byproduct • Contributes to electricity storage option.	• Low overall efficiency • High capital costs	[114,122]
Photoelectrochemical	Hydrogen is produced from water in the presence of sunlight and specialized semiconductors immersed in water-based electrolytes	• Abundant feedstock • O_2 is the only byproduct	• Low conversion efficiency • Non-effective photocatalytic material	[10,114,126]
Photocatalytic	A simple method to produce hydrogen from water in the presence of catalyst and sunlight	• Photocatalyst material directly suspended in to the water • Simple/facile method	• Low yield • Separation of gases • Selection of suitable catalyst • Separation of suspended catalysts	[10,127,128]

In recent years, the structure of the synthesized catalyst and the hydrogen evolution activities have been investigated theoretically using density functional theory (DFT) [129]. In this regard, theoretical studies of metal chalcogenide materials have been conducted. In a recent paper, Som et al. investigated the structural property of ZrS_2, Janus ZrSSe,

and ZrSe$_2$ and their catalytic activity from hydrogen evolution reactions [130]. From these calculations, they found that ZrS$_2$ possessed a larger bandgap energy of 1.58 eV, whereas ZrSSe and ZrSe$_2$ exhibited bandgap energies of 1.08 eV and 0.84 eV, respectively. In addition, Janus ZrSSe (DG $\frac{1}{4}$ 1:19 eV; DG: Gibbs free energy) was found to be the optimal catalyst [130] among the materials studied. Another study examined the electronic and optical properties and the potential applications of 2-D MoSe$_2$/SnS$_2$ van der Waals heterojunction as a photocatalyst for overall water splitting. The DFT calculations showed that the MoSe$_2$/SnS$_2$ heterostructure, as a direct Z-scheme photocatalyst, effectively absorbs visible light. The separation efficiency of photo-induced carriers was enhanced due to the induced built-in electric field. Moreover, when compared with the MoSe$_2$ and SnS$_2$ monolayers, the absorption intensity of the MoSe$_2$/SnS$_2$ heterojunction was reinforced in the visible light region [131].

Park et al. worked on Nb-, Ta-, and Bi-based oxides/chalcogenides. They studied the crystal structure, band dispersion, effective masses of the charge carriers, band alignment, and pH dependence of these materials for hydrogen production and CO$_2$ reduction. They concluded that Bi-based chalcogenide materials, (KBiO$_2$ and KBiS$_2$) showed good performance over a wide range of pH conditions. In addition, the incorporation of chalcogenide narrows the bandgap and reduces the effective mass of the charge carriers when compared with their oxide counterparts [132]. Although these theoretical studies provide guidance toward the identification of materials required for efficient water splitting, it is necessary to test materials. The following sections summarize the reports of hydrogen evolution.

3.1. Photoelectrochemical Hydrogen Evolution

Electrochemical water splitting is a sustainable method for producing hydrogen on a large scale [133]. In photoelectrochemical hydrogen evolution, semiconductor material(s) are immersed in a water-based electrolyte and an external electric power/voltage is applied to dissociate water as hydrogen and oxygen molecules in the presence of a light source [126]. Electrochemical and photoelectrochemical hydrogen evolution have received much attention due to the fact that (i) the generation of O$_2$ and H$_2$ occurs at separate electrodes (Figure 28), which eliminates the separation issue(s), and (ii) the potential for operation under ambient conditions [134].
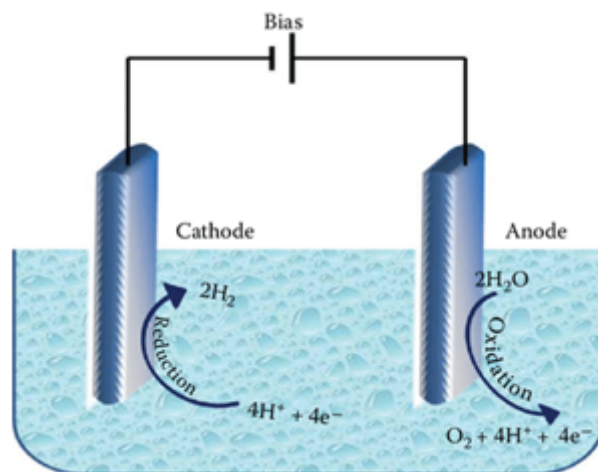
Figure 28. Schematic illustration of the experimental setup of electrochemical water splitting.

Fujishima and Honda first described the photoelectrochemical cell (PEC) splitting of water using a crystalline titanium dioxide anode and a platinum cathode under ultraviolet (UV) irradiation and an external bias [24,135]. The anodic and cathodic reactions are as indicated below [136].

Anode: $2\,H_2O \rightarrow O_2 + 4\,H^+ + 4\,e^-$
Cathode: $2\,H_2O + 4\,H^+ + 4\,e^- \rightarrow 2\,H_2 + 2\,O^{2-}$

Overall reaction: $2\,H_2O \rightarrow 2\,H_2 + O_2$
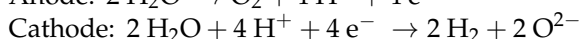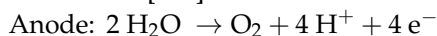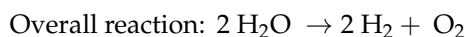
Different studies have been conducted in the field of electrochemical water splitting wherein Pt- and Ru-based materials [137] were used as electrocatalysts for the hydrogen evolution reaction (HER) and oxygen evolution reaction (OER), respectively. In recent years, TMCs have been used. Ahn et al. used CoS_2/rGO (2.3 mg/mL GO) hybrid materials that exhibited high electrocatalytic activity for hydrogen evolution reaction with an over potential of −150 mV versus RHE [138]. In another study, an impressive activity was attributed to the superior electrochemical performance of the Mo–CoS_x skeleton, and the special configuration between MoS_2 and CoS_x, which provide more active sites [139]. Apart from these studies, there have been several metal chalcogenide materials that have been utilized for electrochemical hydrogen evolution, which are summarized in the Table 3 below.

Table 3. Comparison of electrochemical hydrogen evolution by using different TMC photocatalysts.

Material	Current Density	Over Potential	Photocurrent	Other Condition(s)	References
MoS_2	10 mAcm^{-2}	173 mV	109.81 mVdec^{-1}	Nafion resin	[140]
$MoSe_2$	10 mAcm^{-2}	208 mV	65.92 mVdec^{-1}	Nafion resin	[140]
$MoTe_2$	10 mAcm^{-2}	283 mV	102.06 mVdec^{-1}	Nafion resin	[140]
MoS_2/candle soot/Ni foam	10 mAcm^{-2}	56 mV	NA	1.0 M KOH	[108]
3D/2D TiO_2/$MoSe_2$	1.40 mAcm^{-2} 10 mA/cm^{-2}	NA	NA	1.0 M NaOH	[141]
2D MoS_2/$MoSe_2$	147 μmol of H_2 in ∼50 min.	NA	NA	Wide pH conditions	[142]
Amorphous-RuS_2	10 mAcm^{-2}	141 mV	65.6 mVdec^{-1}	0.5 M H_2SO_4	[143]
MoS_2/TiO_2	10 mAcm^{-2}	170 mV	70 mVdec^{-1}	0.5 M H_2SO_4	[118]
GO/NiS_2	10 mAcm^{-2}	57 mV-HER 294 mV-OER	NA	1.0 M KOH	[144]
PU@PANI@FeS_2	10 mAcm^{-2} 50 mAcm^{-2}	266 mV 372 mV	NA	0.5M H_2SO_4	[145]
Cu_xS	NA	–90 mV	100 mVdec^{-1}	0.5 M H_2SO_4	[146]
CoS/MoS_2	NA	−147 mV	126 mVdec^{-1}		[147]
Carbon/Co_3S_4	10 mVcm^{-2}	250 mV and 140 mV for OER and HER	NA	1.0 M KOH	[148]
$NiWSe_x$ and $CoWSe_x$	1 mAcm^{-2}	$NiWSe_x$ (231 mV) $CoWSe_x$ (281 mV) and WSe_x (404 mV)	NA	1.0 M KOH	[149]
MoS_2/Pt	0.642 mAcm^{-2}	NA	52 mVdec^{-1} to 32 mVdec^{-1}	0.5 M $H_2S\,O_4$	[150]
G/MoS_2	10 mAcm^{-2}	118 mV	73 mVedec^{-1}	0.5 M H_2SO_4	[151]
NiS/Pd	10 mAcm^{-2}	100 mV	50 mVdec^{-1}	NA	[152]
$Zn_xCo_{1-x}Se_2$	10 mAcm^{-2}	196 mV-HER 308 mV-OER	NA	HER—acid media OER—alkaline media	[153]
Mo/CoSe	100 mAcm^{-2}	186.1 mV	58.7 mV dec^{-1}	0.5 M H_2SO_4	[154]
MoS_2/graphene	1000 mAcm^{-2}	250 mV	43.3 mVdec^{-1}	0.5 M H_2SO_4	[47]
NiS_2	10 mA/cm^{-2}	302 mV	NA	Nafion ethanol solution	[155]
GaSe	−9.3 μAcm^{-2} 83.4 μAcm^{-2}	+1.23 V vs. RHE	NA	0.5 M H_2SO_4	[156]
1T-MoS_2	10 mAcm^{-2}	240 mV	68 mVdec^{-1}	1 M KOH	[157]
CoSe/$MoSe_2$	10 mAcm^{-2}	192 and 115 mV in acidic and alkaline	NA	Nafion ethanol solution	[158]

NA—Not Available.

3.2. Photocatalytic Hydrogen Evolution

Solar-assisted photocatalytic hydrogen evolution is an attractive technique to generate hydrogen and oxygen, because water and sunlight are abundant and renewable. Furthermore, the photocatalytic process can occur at ambient conditions [14]. Semiconductor materials are used as photocatalysts and their band structure consists of a filled valance band and an empty conduction band separated by a finite bandgap. Irradiation with incident energy greater than or equal to the bandgap of a material leads to excitation of electrons from the valence band to the conduction band edge [159–161]. This leaves holes in the valence band. These photoexcited electrons and holes are potent reducing and oxidizing agents and may react with adsorbed moieties on the surface of the photocatalytic material or may recombine to generate heat [9,136].

Photocatalytic reactions can be classified into two major categories that include uphill reaction, where the Gibbs free energy (ΔG^o) is positive, or downhill reaction, where the (ΔG^o) is negative (Figure 29). In this process, water molecules splitting into H_2 and O_2, are accompanied by a large positive change in the Gibbs free energy (i.e., an uphill

reaction) [130]. During this process, light energy is transformed into chemical energy in a similar manner as the photosynthesis process. Therefore, this reaction is called artificial photosynthesis [136,162].
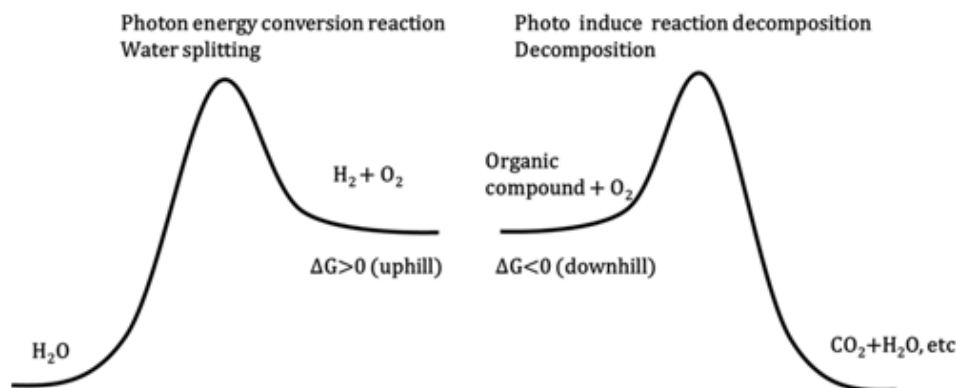
Figure 29. Types of photocatalytic reactions. Reproduced with permission from [130].

The photocatalytic hydrogen evolution through water splitting is a green route and has received significant attention toward simultaneously solving the current global environmental pollution and energy crisis [128]. Various photocatalysts have been well developed for the generation of hydrogen whereas TiO_2 is still considered as a golden standard due to its exceptional stability under irradiation conditions, ease of synthesis, and cost [163]. However, a big disadvantage of TiO_2 is that it requires UV light to be activated, thus limiting its utility since visible light cannot be used. Hence, other oxide and chalcogenide materials are constantly being explored and evaluated for photocatalytic hydrogen production. In addition, ZnO [33], mixed oxides [164], metal chalcogenides such as CdS [165], WS_2 [166], g-C_3N_4 [30], and $CdLa_2S_4$ [34] have also been utilized for the hydrogen evolution reaction.

3.2.1. Principle and Mechanism of Photocatalytic Hydrogen Evolution

In general, photocatalytic hydrogen evolution reaction takes place through three major steps. The first step is the absorption of light by a catalyst to create exciton pair containing electrons and holes. In the second step, the excitons may separate and migrate to the surface of the photocatalyst, and finally, in the third step, the surface reactions take place. The electrons will reduce the protons to generate hydrogen molecules, and holes oxidize water molecules to produce oxygen, as illustrated in the Figure 30 below [167].

Figure 30. Schematic illustration of the process involved during water splitting with the photocatalyst under the illumination of sunlight.

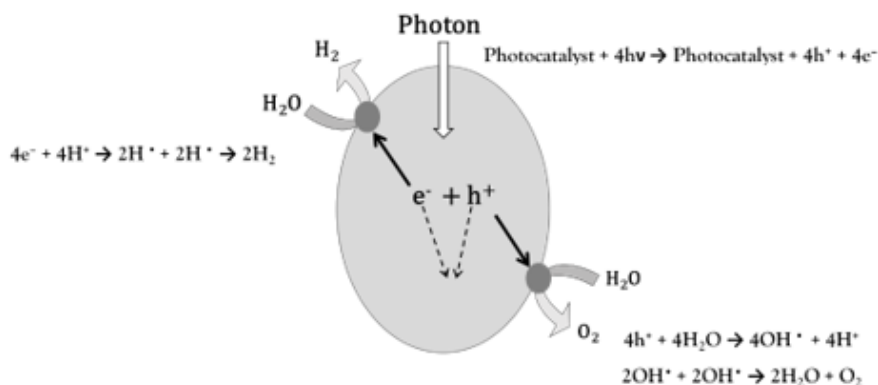The primary reactions (1–4) occurring during the process are listed below, and as indicated, the overall reaction involves four electrons. Table 4 lists the different metal chalcogenide materials used for hydrogen production and the amount of hydrogen evolved.
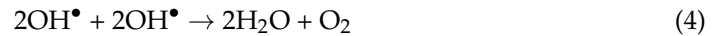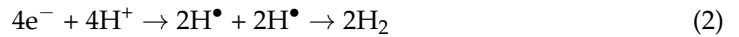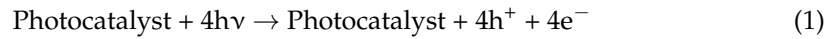
$$Photocatalyst + 4h\nu \rightarrow Photocatalyst + 4h^+ + 4e^- \tag{1}$$

$$4e^- + 4H^+ \rightarrow 2H^\bullet + 2H^\bullet \rightarrow 2H_2 \tag{2}$$

$$4h^+ + 4H_2O \rightarrow 4OH^\bullet + 4H^+ \tag{3}$$

$$2OH^\bullet + 2OH^\bullet \rightarrow 2H_2O + O_2 \tag{4}$$

Table 4. Photocatalytic hydrogen evolution by using different TMC photocatalysts, the experimental conditions used, and the respective references.

Materials	Amount of Hydrogen Evolved	Light Source	Co-Catalyst	Scavenging Agents/Other Chemicals Used	Reference
SnS_2	1.06 mmol h^{-1} g^{-1}	UV–Visible	NA	Na_2S and Na_2SO_3	[38]
$Te/SnS_2/Ag$	332.4 and 166.2 µmol h^{-1} for H_2 and O_2	UV–Visible	NA	-	[168]
SnS_2/g-C_3N_4	972.6 µmol h^{-1}g^{-1}	Visible	Pt	Triethanolamine	[169]
CdS/WS_2	0.42 mmol h^{-1}	Visible	NA	Lactic acid	[166]
NiS /CdS DETA	230 µmolh^{-1}	Visible	NA	-	[170]
$CdS/ZnO/GO$, $CdS/Al_2O_3/GO$	22.12 mmol h^{-1}g^{-1}	500 W Phoenix tungsten halogen lamp	Pt	Na_2SO_3 and Na_2S	[171]
$MoS_2/RGO/CdS$	99 µmol h^{-1}	Visible	NA	Lactic acid	[42]
MoS_2/G	1.80 mmol h^{-1}	Visible	NA	Na_2S and $Na_2S_2O_3$	[172]
Eosin Y/NiS_x/G	0.34 mmol h^{-1}	Visible	NA	Triethanolamine	[22]
$NiS/CdS/ZnS$	574 µmol h^{-1}	Visible	NA	$Na_2S/Na_2S_2O_3$	[173]
MoS_2	110 µmol h^{-1}	Visible	La^{3+}	Methanol	[109]
CuS–MoS_2–1T	9648.7 µmol g^{-1}h^{-1}	UV–Visible	NA	0.3 M Na_2SO_3	[174]
WS_2/TiO_2	596.4 µmolg^{-1}	Visible	Pt	1 wt. % of WS_2/TiO_2	[31]
$ZnIn_2S_4/g$-C_3N_4	450 µmol g^{-1}h^{-1}	Visible	NA	Triethanolamine	[175]
$WSe_2/ Zn_{0.1}Cd_{0.9}S$	147.32 µmol g^{-1}h^{-1}	Visible	NA	Lactic acid	[176]
$NiCo/Zn_{0.5}Cd_{0.5}S$	34.7 mmol g^{-1}h^{-1}	UV–Visible	NA	Na_2S and Na_2SO_3	[177]
$NiSe_2/RP$	1968.8µmol g^{-1}h^{-1}	UV–Visible	NA	Na_2S and Na_2SO_3	[178]
CdS	3072 µmol g^{-1}h^{-1}	UV–Visible	NA	Na_2S and Na_2SO_3	[179]
$ZnS/CdS/Cd_{0.5}Zn_{0.5}S/MoS_2$	50.65 mmol g^{-1}h^{-1}	Visible	NA	Lactic acid, Na2S, and Na_2SO_3	[117]
$Cd_xMo_{1-x}Se$	911.1 mol in 7 h	Visible	NA	Na_2S and Na_2SO_3	[180]
$MoS_2/CdIn_2S_4$	1868.19 µmol g^{-1}h^{-1}	UV–Visible	NA	Na_2S and Na_2SO_3	[181]
$MoS_2/CoSe_2/1D$-CdS	191.5 mmol g^{-1}h^{-1}	UV–Visible	NA	Lactic acid	[182]
$NiS/CQDs/ZnIn_2S_4$	28.2 µmol h^{-1}	Visible	NA	Trimethylamine	[183]
$NiSe_2/CdS$	167.1 mmol g^{-1}h^{-1}	Visible	NA		[184]
$NiS/ZnIn_2S_4$	5.0 µmol h^{-1}	Visible	NA	Methanol and lactic acid	[185]
1T-MoS_2-ZnCoS	15.47 mmol h^{-1} g^{-1}	UV–Visible	NA	Trimethylamine, Eosin Y, and acetonitrile	[120]
CdS/SnS_2	20.2 mmol h^{-1} g^{-1}	UV–Visible	NA	Lactic acid	[186]
ZnO−ZnS−Cu_2S	436 µmol h^{-1} g^{-1}	Visible	NA	Na_2S and Na_2SO_3	[187]
ZnS films	5202.4 µmol h^{-1} g^{-1}	UV	NA	Na_2SO_3	[188]
CoS_2/TiO_2	2.55 mmol g^{-1}	UV	NA	Methanol	[105]
SnS_2/TiO_2	195.0 µmol g^{-1}	Visible	NA	Methanol	[106]
(NC@Co-NCT)/(CdS)	3.8 mmol h^{-1} g^{-1}	Visible	NA	lactic acid	[189]
CdSe QDs/g-C_3N_4	192.3 µmol h^{-1}	Visible	H_2PtCl_6	Triethanolamine, Na_2S, and Na_2SO_3	[190]

3.2.2. Measurements of the Rate of Hydrogen Evolution (Quantum Yield)

Generally, the rate of hydrogen evolution is denoted with the unit of µmolh^{-1}g^{-1}, which indicates the number of moles of hydrogen evolved in unit time using a unit amount of catalyst. This amount depends on several experimental conditions such as reaction vessel, light source, intensity of radiation, amount of catalyst, sacrificial agent, etc. [120]. However, it is noteworthy to mention here that there are inconsistencies among researchers in reporting the rate of hydrogen evolution and hence care must be exercised in making

comparisons from one report to another. To provide a general quantification, quantum yield measurement is important in photolytic reactions to remove any variations in experimental conditions and for making meaningful comparisons among different photocatalysts and provide consistent benchmarking. Although the number of incident photons can be measured using a thermopile, it is difficult to determine the actual number of photons absorbed by a photocatalyst because of scattering and some reflection in a dispersed system. Photocatalytic/luminescence materials convert excitation energy into photons, and this conversion is usually not 100% efficient due to various losses through alternative deactivation paths. Therefore, two additional parameters such as the quantum yield (QY) and the quantum (energy) efficiency [191] have to be defined. In preparative photochemistry, the QY is defined as the product yield of a reaction calculated by the number of moles of reactant reacted per unit time. This type of QY has been preferred as it can be measured with small expenditure. However, it depends on the time section of the reaction in which it is determined. Therefore, the QY can be considered to be an apparent quantum yield (AQY), and this yield is mainly dependent on the time at which they are considered [192]. AQY is the ratio between the number of reacted electrons and the number of incident photons, and is used for the quantification of hydrogen evolution. The following Equation (5) explains the percentage of AQY calculation [9].

$$AQY(\%) = \frac{\text{the number of reacted electrons}}{\text{the number of incident photons}} \times 100\% \tag{5}$$

$$= \frac{\text{the number of evolved } H_2 \text{ molecules } \times 2}{\text{the number of incident photons}} \times 100\%$$

The turnover frequency (TOF) of photocatalysts based on the amount of a particular molecule can be calculated using Equation (6) [193]:

$$TOF = \frac{\text{moles of produced hydrogen}}{\text{moles of a particular molecule in photocatalyst } \times \text{ reaction time (h)}} \tag{6}$$

Mangiri R. et al. used a dual co-catalyst of $MoS_2/CoSe_2$ on CdS for the hydrogen evolution reaction (Figure 31), and the system evolved a higher rate of hydrogen with the yield of 191.5 mmol g^{-1} h^{-1}, which was 76.6 times higher than that of pristine CdS [182].
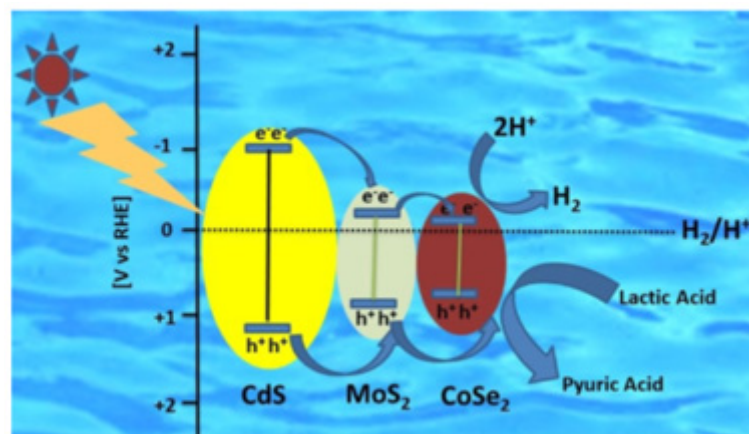
Figure 31. Schematic diagram of the mechanism of the hydrogen evolution reduction (HER) process. Reproduced with permission from [182].

In their study, CdS was used as a semiconductor, which can harvest the light and eject electrons from the conduction band of CdS to its valance band. Then, the photogenerated electrons in the conduction band of CdS can be easily transferred to MoS_2 and $CoSe_2$ due to the favorable band edge positions of the three materials. Thus, the rate of charge-carrier recombination is minimized and photocatalytic activity is enhanced in the

composite photocatalyst in comparison to the pristine CdS materials. Here, the MoS_2 and $CoSe_2$ act as reactive sites to produce hydrogen. The holes produced can react with lactic acid and oxidize it to pyruvic acid [182].

In a different study, Riaz et al. used 3% La^{3+} doped MoS_2, and it exhibited an enhanced photocatalytic performance for hydrogen evolution with a 5.2 times higher hydrogen evolution rate compared with pure MoS_2 [109] (Figure 32). This has been attributed to the presence of trapping energy levels formed below the conduction band of MoS_2 due to the lanthanum ion-doping and minimizing recombination of electrons and holes. Surface adsorbed La^{3+} atoms also ensured the rapid transfer of electrons from MoS_2 to capture protons for H_2 production [109].
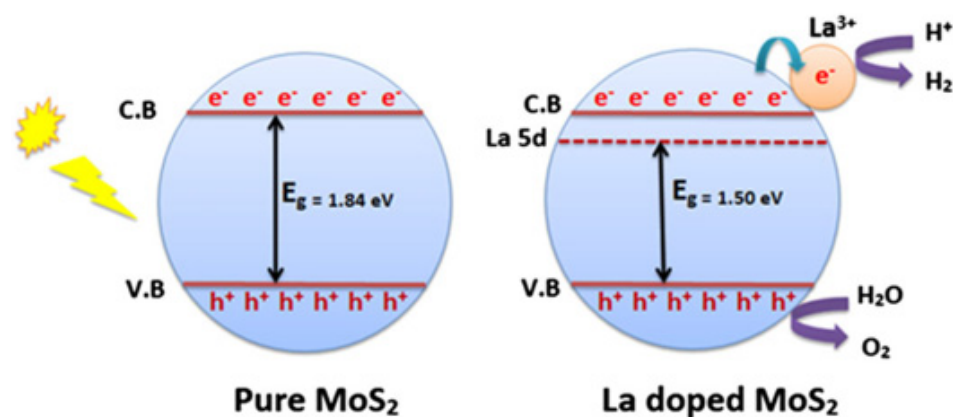

Figure 32. Schematic diagram of the proposed reaction mechanism for H_2 production using the La-MoS_2 photocatalyst. Reproduced with permission from [109].

Transition metal chalcogenides with and without incorporation of other materials such as metals [168], graphene [172], graphene oxide [42], carbon nitrides [169], dyes [194], and metal oxides [33] have been utilized for hydrogen production (Table 4). It can be seen that the use of composite photocatalysts, in general, leads to a higher rate of hydrogen production than the pristine transition metal chalcogenides. This has been attributed to the presence of heterojunctions that favor vectorial transfer of electrons that minimize electron-hole recombination.

4. Summary

This review details the recent approaches to the hydrogen evolution reaction using TMCs, which are being considered as potential catalysts for the production of an energy carrier, hydrogen, due to their favorable electronic and optical properties. The different synthesis methods of TMCs and their characteristic properties reported in the literature are discussed in detail, providing guidance for interested researchers to explore TMCs as exploratory materials. Furthermore, the catalytic activities of TMCs for hydrogen evolution reactions were also elaborated herein. Overall, this review provides an overview of the recent approaches to hydrogen production using TMCs.

Author Contributions: Conceptualization, Y.S.; Methodology, S.S. and E.Y.; Investigation, S.S., Y.S., P.R., D.V. and R.K.; Resources, Y.S., P.R., D.V. and R.K.; Original draft preparation, S.S. and E.Y.; Writing—review & editing, S.S., E.Y., Y.S. and R.K.; Supervision, Y.S., P.R. and D.V. All authors have read and agreed to the published version of the manuscript.

Institutional Review Board Statement: Not applicable.

Informed Consent Statement: Not applicable.

Conflicts of Interest: There is no conflict of interest.

References

1. Ma, Q.; Hu, C.; Liu, K.; Hung, S.-F.; Ou, D.; Chen, H.M.; Fu, G.; Zheng, N. Identifying the electrocatalytic sites of nickel disulfide in alkaline hydrogen evolution reaction. *Nano Energy* **2017**, *41*, 148–153. [CrossRef]
2. Bai, J.; Meng, T.; Guo, D.; Wang, S.; Mao, B.; Cao, M. Co9S8@MoS₂ Core–Shell Heterostructures as Trifunctional Electrocatalysts for Overall Water Splitting and Zn–Air Batteries. *ACS Appl. Mater. Interfaces* **2018**, *10*, 1678–1689. [CrossRef] [PubMed]
3. Naik, S.G.; Rabinal, M.H.K. Molybdenum Disulphide Heterointerfaces as Potential Materials for Solar Cells, Energy Storage, and Hydrogen Evolution. *Energy Technol.* **2020**, *8*. [CrossRef]
4. Feng, K.; Huang, D.; Li, L.; Wang, K.; Li, J.; Harada, T.; Ikeda, S.; Jiang, F. MoSx-CdS/Cu₂ZnSnS₄-based thin film photocathode for solar hydrogen evolution from water. *Appl. Catal. Environ.* **2020**, *268*, 118438. [CrossRef]
5. Züttel, A. Hydrogen storage methods. *Naturwissenschaften* **2004**, *91*, 157–172. [CrossRef] [PubMed]
6. Züttel, A. Materials for hydrogen storage. *Mater. Today* **2003**, *6*, 24–33. [CrossRef]
7. Paquin, F.; Rivnay, J.; Salleo, A.; Stingelin, N.; Silva, C. Multi-phase semicrystalline microstructures drive exciton dissociation in neat plastic semiconductors. *J. Mater. Chem.* **2015**, *3*, 10715–10722. [CrossRef]
8. Lin, L.; Sherrell, P.; Liu, Y.; Lei, W.; Zhang, S.; Zhang, H.; Wallace, G.G.; Chen, J. Engineered 2D Transition Metal Dichalcogenides— A Vision of Viable Hydrogen Evolution Reaction Catalysis. *Adv. Energy Mater.* **2020**, *10*. [CrossRef]
9. Kudo, A.; Miseki, Y. Heterogeneous photocatalyst materials for water splitting. *Chem. Soc. Rev.* **2009**, *38*, 253–278. [CrossRef] [PubMed]
10. Nikolaidis, P.; Poullikkas, A. A comparative overview of hydrogen production processes. *Renew. Sustain. Energy Rev.* **2017**, *67*, 597–611. [CrossRef]
11. Dincer, I. Green methods for hydrogen production. *Int. J. Hydrogen Energy* **2012**, *37*, 1954–1971. [CrossRef]
12. Ma, L.-C.; Dominguez, B.C.; Kazantzis, N.K.; Ma, Y.H. Integration of membrane technology into hydrogen production plants with CO₂ capture: An economic performance assessment study. *Int. J. Greenh. Gas Control.* **2015**, *42*, 424–438. [CrossRef]
13. Luo, P.; Zhang, H.; Liu, L.; Zhang, Y.; Deng, J.; Xu, C.; Hu, N.; Wang, Y. Targeted Synthesis of Unique Nickel Sulfide (NiS, NiS₂) Microarchitectures and the Applications for the Enhanced Water Splitting System. *ACS Appl. Mater. Interfaces* **2017**, *9*, 2500–2508. [CrossRef] [PubMed]
14. Leung, D.Y.C.; Fu, X.; Wang, C.; Ni, M.; Leung, M.K.H.; Wang, X.; Fu, X. Hydrogen Production over Titania-Based Photocatalysts. *ChemSusChem* **2010**, *3*, 681–694. [CrossRef] [PubMed]
15. Yin, Y.; Jin, Z.; Hou, F. Enhanced solar water-splitting efficiency using core/sheath heterostructure CdS/TiO₂ nanotube arrays. *Nanotechnology* **2007**, *18*, 495608. [CrossRef]
16. Kim, S.B.; Hong, S.C. Kinetic study for photocatalytic degradation of volatile organic compounds in air using thin film TiO₂ photocatalyst. *Appl. Catal. Environ.* **2002**, *35*, 305–315. [CrossRef]
17. Matthews, R. Photooxidative degradation of coloured organics in water using supported catalysts. TiO₂ on sand. *Water Res.* **1991**, *25*, 1169–1176. [CrossRef]
18. Chakrabarti, S.; Dutta, B.K. Photocatalytic degradation of model textile dyes in wastewater using ZnO as semiconductor catalyst. *J. Hazard. Mater.* **2004**, *112*, 269–278. [CrossRef]
19. Mugunthan, E.; Saidutta, M.B.; JagadeeshBabu, P.E. Photocatalytic degradation of diclofenac using TiO₂–SnO₂ mixed oxide catalysts. *Environ. Technol.* **2019**, *40*, 929–941. [CrossRef] [PubMed]
20. Kim, H.G.; Hwang, D.W.; Kim, J.; Kim, Y.G.; Lee, J.S. Highly donor-doped (110) layered perovskite materials as novel photocatalysts for overall water splitting. *Chem. Commun.* **1999**, *2*, 1077–1078. [CrossRef]
21. Kanazawa, T.; Nozawa, S.; Lu, D.; Maeda, K. Structure and Photocatalytic Activity of PdCrOx Cocatalyst on SrTiO₃ for Overall Water Splitting. *Catalysts* **2019**, *9*, 59. [CrossRef]
22. Kong, C.; Min, S.; Lu, G. Dye-Sensitized NiSx Catalyst Decorated on Graphene for Highly Efficient Reduction of Water to Hydrogen under Visible Light Irradiation. *ACS Catal.* **2014**, *4*, 2763–2769. [CrossRef]
23. Zhang, W.; Xiao, X.; Zeng, X.; Li, Y.; Zheng, L.; Wan, C. Enhanced photocatalytic activity of TiO₂ nanoparticles using SnS₂/RGO hybrid as co-catalyst: DFT study and photocatalytic mechanism. *J. Alloys Compd.* **2016**, *685*, 774–783. [CrossRef]
24. Jafari, T.; Moharreri, E.; Amin, A.S.; Miao, R.; Song, W.; Suib, S.L. Photocatalytic Water Splitting—The Untamed Dream: A Review of Recent Advances. *Molecules* **2016**, *21*, 900. [CrossRef]
25. Li, Y.; Zhou, X.; Xing, Y. In situ thermal-assisted loading of monodispersed Pt nanoclusters on CdS nanoflowers for efficient photocatalytic hydrogen evolution. *Appl. Surf. Sci.* **2020**, *506*, 144933. [CrossRef]
26. Zheng, L.; Zhang, W.; Xiao, X. Preparation of titanium dioxide/tungsten disulfide composite photocatalysts with enhanced photocatalytic activity under visible light. *Korean J. Chem. Eng.* **2015**, *33*, 107–113. [CrossRef]
27. Wang, Q.; Huang, J.; Sun, H.; Ng, Y.H.; Zhang, K.-Q.; Lai, Y. MoS₂ Quantum Dots@TiO₂ Nanotube Arrays: An Extended-Spectrum-Driven Photocatalyst for Solar Hydrogen Evolution. *ChemSusChem* **2018**, *11*, 1708–1721. [CrossRef]
28. Ali, A.; Oh, W.-C. Photocatalytic Performance of CoS₂-Graphene-TiO₂ Ternary Composites for Reactive Black B (RBB) Degradation. *J. Korean Ceram. Soc.* **2017**, *54*, 308–313. [CrossRef]

29. Li, Y.; Wang, H.; Xie, L.; Liang, Y.; Hong, G.; Dai, H. MoS$_2$ Nanoparticles Grown on Graphene: An Advanced Catalyst for the Hydrogen Evolution Reaction. *J. Am. Chem. Soc.* **2011**, *133*, 7296–7299. [CrossRef]

30. He, K.; Xie, J.; Li, M.; Li, X. In situ one-pot fabrication of g-C3N4 nanosheets/NiS cocatalyst heterojunction with intimate interfaces for efficient visible light photocatalytic H2 generation. *Appl. Surf. Sci.* **2018**, *430*, 208–217. [CrossRef]

31. Jing, D.; Guo, L. WS$_2$ sensitized mesoporous TiO$_2$ for efficient photocatalytic hydrogen production from water under visible light irradiation. *Catal. Commun.* **2007**, *8*, 795–799. [CrossRef]

32. Wang, Y.; Yang, X.; Wang, Z.; Lv, X.; Jia, H.; Kong, J.; Yu, M. CdS and SnS$_2$ nanoparticles co-sensitized TiO$_2$ nanotube arrays and the enhanced photocatalytic property. *J. Photochem. Photobiol. Chem.* **2016**, *325*, 55–61. [CrossRef]

33. Ma, D.; Shi, J.-W.; Zou, Y.; Fan, Z.; Ji, X.; Niu, C. Highly Efficient Photocatalyst Based on a CdS Quantum Dots/ZnO Nanosheets 0D/2D Heterojunction for Hydrogen Evolution from Water Splitting. *ACS Appl. Mater. Interfaces* **2017**, *9*, 25377–25386. [CrossRef] [PubMed]

34. Yuan, Y.-P.; Cao, S.-W.; Yin, L.-S.; Xu, L.; Xue, C. NiS$_2$ Co-catalyst decoration on CdLa$_2$S$_4$ nanocrystals for efficient photocatalytic hydrogen generation under visible light irradiation. *Int. J. Hydrogen Energy* **2013**, *38*, 7218–7223. [CrossRef]

35. Sun, B.; Liu, A.; Li, J.; Wang, J.; Wang, S. Development of novel highly stable synergistic quaternary photocatalyst for the efficient hydrogen evolution reaction. *Appl. Surf. Sci.* **2020**, *510*, 145498. [CrossRef]

36. Makwana, N.M.; Tighe, C.J.; Gruar, R.I.; McMillan, P.F.; Darr, J.A. Pilot plant scale continuous hydrothermal synthesis of nano-titania; effect of size on photocatalytic activity. *Mater. Sci. Semicond. Process.* **2016**, *42*, 131–137. [CrossRef]

37. Huerta-Flores, A.M.; Torres-Martínez, L.M.; Moctezuma, E.; Singh, A.P.; Wickman, B. Green synthesis of earth-abundant metal sulfides (FeS$_2$, CuS, and NiS$_2$) and their use as visible-light active photocatalysts for H$_2$ generation and dye removal. *J. Mater. Sci. Mater. Electron.* **2018**, *29*, 11613–11626. [CrossRef]

38. Yu, J.; Xu, C.; Ma, F.; Hu, S.-P.; Zhang, Y.-W.; Zhen, L. Monodisperse SnS$_2$ Nanosheets for High-Performance Photocatalytic Hydrogen Generation. *ACS Appl. Mater. Interfaces* **2014**, *6*, 22370–22377. [CrossRef]

39. Xu, K.; Wang, F.; Wang, Z.; Zhan, X.; Wang, Q.; Cheng, Z.; Safdar, M.; He, J. Component-Controllable WS2(1–x)Se2x Nanotubes for Efficient Hydrogen Evolution Reaction. *ACS Nano* **2014**, *8*, 8468–8476. [CrossRef]

40. Voiry, D.; Salehi, M.; Silva, R.; Fujita, T.; Chen, M.; Asefa, T.; Shenoy, V.B.; Eda, G.; Chhowalla, M. Conducting MoS$_2$ Nanosheets as Catalysts for Hydrogen Evolution Reaction. *Nano Lett.* **2013**, *13*, 6222–6227. [CrossRef] [PubMed]

41. Sun, Y.; Liu, C.; Grauer, D.C.; Yano, J.; Long, J.R.; Yang, P.; Chang, C.J. Electrodeposited Cobalt-Sulfide Catalyst for Electrochemical and Photoelectrochemical Hydrogen Generation from Water. *J. Am. Chem. Soc.* **2013**, *135*, 17699–17702. [CrossRef] [PubMed]

42. Li, Y.; Wang, H.; Peng, S. Tunable Photodeposition of MoS$_2$ onto a Composite of Reduced Graphene Oxide and CdS for Synergic Photocatalytic Hydrogen Generation. *J. Phys. Chem. C* **2014**, *118*, 19842–19848. [CrossRef]

43. Liu, J.-H.; Huang, G.-F.; Huang, W.-Q.; Miao, H.; Zhou, B.-X. Morphology-controlled SnS$_2$ nanostructures synthesized by refluxing method with high photocatalytic activity. *Mater. Lett.* **2015**, *161*, 480–483. [CrossRef]

44. Wang, Q.; Lei, Y.; Wang, Y.; Liu, Y.; Song, C.; Zeng, J.; Song, Y.; Duan, X.; Wang, D.; Li, Y. Atomic-scale engineering of chemical-vapor-deposition-grown 2D transition metal dichalcogenides for electrocatalysis. *Energy Environ. Sci.* **2020**, *13*, 1593–1616. [CrossRef]

45. Luo, M.; Liu, Y.; Hu, J.; Liu, H.; Li, J. One-Pot Synthesis of CdS and Ni-Doped CdS Hollow Spheres with Enhanced Photocatalytic Activity and Durability. *ACS Appl. Mater. Interfaces* **2012**, *4*, 1813–1821. [CrossRef] [PubMed]

46. Wang, Y.; Li, L.; Yao, W.; Song, S.; Sun, J.T.; Pan, J.; Ren, X.; Li, C.; Okunishi, E.; Wang, Y.-Q.; et al. Monolayer PtSe2, a New Semiconducting Transition-Metal-Dichalcogenide, Epitaxially Grown by Direct Selenization of Pt. *Nano Lett.* **2015**, *15*, 4013–4018. [CrossRef] [PubMed]

47. Sarwar, S.; Nautiyal, A.; Cook, J.; Yuan, Y.; Li, J.; Uprety, S.; Shahbazian-Yassar, R.; Wang, R.; Park, M.; Bozack, M.J.; et al. Facile microwave approach towards high performance MoS$_2$/graphene nanocomposite for hydrogen evolution reaction. *Sci. China Mater.* **2020**, *63*, 62–74. [CrossRef]

48. Jiao, F.; Yen, H.; Hutchings, G.S.; Yonemoto, B.; Lua, Q.; Kleitz, F. Synthesis, structural characterization, and electrochemical performance of nanocast mesoporous Cu-/Fe-based oxides. *J. Mater. Chem. A* **2014**, *2*, 3065–3071. [CrossRef]

49. Panigrahi, P.K.; Pathak, A. Microwave-assisted synthesis of WS$_2$ nanowires through tetrathiotungstate precursors. *Sci. Technol. Adv. Mater.* **2008**, *9*, 045008. [CrossRef] [PubMed]

50. Liu, H.; Su, Y.; Chen, P.; Wang, Y. Microwave-assisted solvothermal synthesis of 3D carnation-like SnS$_2$ nanostructures with high visible light photocatalytic activity. *J. Mol. Catal. Chem.* **2013**, *378*, 285–292. [CrossRef]

51. Rao, B.G.; Mukherjee, D.; Reddy, B.M. *Novel Approaches for Preparation of Nanoparticles*; Elsevier Inc.: Amsterdam, The Netherlands, 2017; ISBN 9780323461481.

52. Kumar, A. Different Methods Used for the Synthesis of TiO$_2$ Based Nanomaterials: A Review. *Am. J. Nano Res. Appl.* **2018**, *6*, 1–10. [CrossRef]

53. Aliofkhazraei, M. (Ed.) *Handbook of Nanoparticles*; Springer International Publishing: Cham, Switzerland, 2016.

54. Pokrovski, G.S.; Roux, J.; Hazemann, J.-L.; Borisova, A.; Gonchar, A.A.; Lemeshko, M.P. In situ X-ray absorption spectroscopy measurement of vapour-brine fractionation of antimony at hydrothermal conditions. *Miner. Mag.* **2008**, *72*, 667–681. [CrossRef]

55. Gautam, A.K.; Faraz, M.; Khare, N. Enhanced thermoelectric properties of MoS$_2$ with the incorporation of reduced graphene oxide (RGO). *J. Alloys Compd.* **2020**, *838*, 155673. [CrossRef]

56. Bricha, M.; Belmamouni, Y.; Essassi, E.M.; Ferreira, J.; El Mabrouk, K. Surfactant-Assisted Hydrothermal Synthesis of Hydroxyapatite Nanopowders. *J. Nanosci. Nanotechnol.* **2012**, *12*, 8042–8049. [CrossRef]

57. Cao, S.; Liu, T.; Zeng, W.; Hussain, S.; Peng, X.; Pan, F. Synthesis and characterization of flower-like WS_2 nanospheres via a facile hydrothermal route. *J. Mater. Sci. Mater. Electron.* **2014**, *25*, 4300–4305. [CrossRef]

58. Naskar, B.; Dan, A.; Ghosh, S.; Aswal, V.; Moulik, S.P. Revisiting the self-aggregation behavior of cetyltrimethylammonium bromide in aqueous sodium salt solution with varied anions. *J. Mol. Liq.* **2012**, *170*, 1–10. [CrossRef]

59. Vollath, D.; Szabó, D.V. Synthesis of nanocrystalline MoS_2 and WS_2 in a microwave plasma. *Mater. Lett.* **1998**, *35*, 236–244. [CrossRef]

60. Shanmugaratnam, S.; Rasalingam, S. Transition Metal Chalcogenide (TMC) Nanocomposites for Environmental Remediation Application over Extended Solar Irradiation. In *Nanocatalysts*; IntechOpen: London, UK, 2012. [CrossRef]

61. Park, S.; Park, J.; Selvaraj, R.; Kim, Y. Facile microwave-assisted synthesis of SnS_2 nanoparticles for visible-light responsive photocatalyst. *J. Ind. Eng. Chem.* **2015**, *31*, 269–275. [CrossRef]

62. Choubey, S.K.; Tiwary, K.P. Microwave assisted synthesis of CdS nanoparticles for structural and optical characterization. *IJIRSET* **2014**, *3*, 10670–10674.

63. Nethravathi, C.; Rajamathi, J.T.; Rajamathi, M. Microwave-Assisted Synthesis of Porous Aggregates of CuS Nanoparticles for Sunlight Photocatalysis. *ACS Omega* **2019**, *4*, 4825–4831. [CrossRef] [PubMed]

64. Pang, H.; Wei, C.; Li, X.; Li, G.; Ma, Y.; Li, S.; Chen, J.; Zhang, J. Microwave-assisted synthesis of NiS_2 nanostructures for supercapacitors and cocatalytic enhancing photocatalytic H_2 production. *Sci. Rep.* **2014**, *4*, 1–8. [CrossRef]

65. Amaresh, S.; Karthikeyan, K.; Jang, I.-C.; Lee, Y.S. Single-step microwave mediated synthesis of the CoS_2 anode material for high rate hybrid supercapacitors. *J. Mater. Chem. A* **2014**, *2*, 11099–11106. [CrossRef]

66. Liu, B.; Qu, S.; Kou, Y.; Liu, Z.; Chen, X.; Wu, Y.; Han, X.; Deng, Y.; Hu, W.; Zhong, C. In Situ Electrodeposition of Cobalt Sulfide Nanosheet Arrays on Carbon Cloth as a Highly Efficient Bifunctional Electrocatalyst for Oxygen Evolution and Reduction Reactions. *ACS Appl. Mater. Interfaces* **2018**, *10*, 30433–30440. [CrossRef] [PubMed]

67. Ghahremaninezhad, A.; Asselin, E.; Dixon, D.G. Electrodeposition and Growth Mechanism of Copper Sulfide Nanowires. *J. Phys. Chem. C* **2011**, *115*, 9320–9334. [CrossRef]

68. Mammadov, M.N.; Sh Aliyev, A.; Elrouby, M. Electrodeposition of cadmium sulfide. *Int. J. Thin Film Sci. Tec.* **2012**, *1*, 43–53.

69. Huang, J.; Daryadel, S.; Minary-Jolandan, M. Low-Cost Manufacturing of Metal–Ceramic Composites through Electrodeposition of Metal into Ceramic Scaffold. *ACS Appl. Mater. Interfaces* **2019**, *11*, 4364–4372. [CrossRef]

70. Maharana, H.; Basu, A.; Mondal, K. Structural and tribological correlation of electrodeposited solid lubricating Ni-WSe_2 composite coating. *Surf. Coatings Technol.* **2018**, *349*, 328–339. [CrossRef]

71. Safavi, M.S.; Fathi, M.; Charkhesht, V.; Jafarpour, M.; Ahadzadeh, I. Electrodeposition of Co-P Coatings Reinforced by MoS_2 + Y_2O_3 Hybrid Ceramic Nanoparticles for Corrosion-Resistant Applications: Influences of Operational Parameters. *Met. Mater. Trans. A* **2020**, *51*, 6740–6758. [CrossRef]

72. Jayakrishnan, D.S. *Electrodeposition: The Versatile Technique for Nanomaterials*; Woodhead Publishing Limited: Sawston, UK, 2012.

73. Aruna, S.; Bindu, C.; Selvi, V.E.; Grips, V.W.; Rajam, K. Synthesis and properties of electrodeposited Ni/ceria nanocomposite coatings. *Surf. Coatings Technol.* **2006**, *200*, 6871–6880. [CrossRef]

74. Shariza, S.; Anand, T.J.S. Effect of deposition time on the structural and optical properties of molybdenum chalcogenides thin films. *Chalcogenide Lett.* **2011**, *8*, 529–539.

75. Chen, Y.-C.; Huang, Y.-S.; Huang, H.; Su, P.-J.; Perng, T.-P.; Chen, L.-J. Photocatalytic enhancement of hydrogen production in water splitting under simulated solar light by band gap engineering and localized surface plasmon resonance of $Zn_xCd_{1-x}S$ nanowires decorated by Au nanoparticles. *Nano Energy* **2020**, *67*, 104225. [CrossRef]

76. Sankapal, B.R.; Mane, R.S.; Lokhande, C.D. Successive ionic layer adsorption and reaction (SILAR) method for the deposition of large area (~10 cm^2) tin disulfide (SnS_2) thin films. *Mater. Res. Bull.* **2000**, *35*, 2027–2035. [CrossRef]

77. Pathan, H.M.; Lokhande, C.D. Deposition of metal chalcogenide thin films by successive ionic layer adsorption and reaction (SILAR) method. Bull. *Mater. Sci* **2004**, *27*, 85–111.

78. Leskell, M. Deposition of manganese-doped successive ionic layer adsorption zinc sulfide thin films by the and reaction (SILAR) method. *Thin Solid Film.* **1995**, *263*, 79–84.

79. Lindroos, S.; Kanniainen, T.; Leskelä, M. Growth of zinc sulfide thin films by the successive ionic layer adsorption and reaction (SILAR) method on polyester substrates. *Mater. Res. Bull.* **1997**, *32*, 1631–1636. [CrossRef]

80. Valkonen, M.P.; Kanniainen, T.; Lindroos, S.; Leskelä, M.; Rauhala, E. Growth of ZnS, CdS and multilayer ZnS/CdS thin films by SILAR technique. *Appl. Surf. Sci.* **1997**, *115*, 386–392. [CrossRef]

81. Aditha, S.K.; Kurdekar, A.D.; Chunduri, L.A.A.; Patnaik, S.; Kamisetti, V. Aqueous based reflux method for green synthesis of nanostructures: Application in CZTS synthesis. *MethodsX* **2016**, *3*, 35–42. [CrossRef] [PubMed]

82. Phuruangrat, A.; Thoonchalong, P.; Thongtem, S.; Thongtem, T. Synthesis of cus with different morphologies by refluxing method: Nanopaticles in clusters and nanoflakes in sponge-like clusters. *Chalcogenide Lett.* **2012**, *9*, 421–426.

83. Wang, L.-C.; Bao, S.-K.; Luo, J.; Wang, Y.-H.; Nie, Y.-C.; Zou, J.-P. Efficient exfoliation of bulk MoS_2 to nanosheets by mixed-solvent refluxing method. *Int. J. Hydrogen Energy* **2016**, *41*, 10737–10743. [CrossRef]

84. Phuruangrat, A.; Karthik, K.; Kuntalue, B.; Dumrongrojthanath, P.; Thongtem, S.; Thongtem, T.; Yai, H.; Nadu, T.; Science, M. Refuxing synthesis and characterization of zns nanoparticles and their photocatalytic properties. *Chalcogenide Lett.* **2019**, *16*, 387–393.

85. Dai, Z.; Zang, X.; Yang, J.; Sun, C.; Si, W.; Huang, W.; Dong, X. Template Synthesis of Shape-Tailorable NiS$_2$ Hollow Prisms as High-Performance Supercapacitor Materials. *ACS Appl. Mater. Interfaces* **2015**, *7*, 25396–25401. [CrossRef] [PubMed]

86. Li, J.; Yang, X.; Liu, Y.; Huang, B.; Wu, R.; Zhang, Z.; Zhao, B.; Ma, H.; Dang, W.; Wei, Z.; et al. General synthesis of two-dimensional van der Waals heterostructure arrays. *Nat. Cell Biol.* **2020**, *579*, 368–374. [CrossRef] [PubMed]

87. Gong, Y.; Lin, J.; Wang, X.; Shi, G.; Lei, S.; Lin, Z.; Zou, X.; Ye, G.; Vajtai, R.; Yakobson, B.I.; et al. Vertical and in-plane heterostructures from WS$_2$/MoS$_2$ monolayers. *Nat. Mater.* **2014**, *13*, 1135–1142. [CrossRef] [PubMed]

88. Hao, S.; Yang, B.; Gao, Y. Orientation-specific transgranular fracture behavior of CVD-grown monolayer MoS$_2$ single crystal. *Appl. Phys. Lett.* **2017**, *110*, 153105. [CrossRef]

89. Kim, S.; Kwak, J.; Ciobanu, C.V.; Kwon, S. Recent Developments in Controlled Vapor-Phase Growth of 2D Group 6 Transition Metal Dichalcogenides. *Adv. Mater.* **2019**, *31*, e1804939. [CrossRef]

90. Tan, H.; Fan, Y.; Zhou, Y.; Chen, Q.; Xu, W.; Warner, J.H. Ultrathin 2D Photodetectors Utilizing Chemical Vapor Deposition Grown WS$_2$ With Graphene Electrodes. *ACS Nano* **2016**, *10*, 7866–7873. [CrossRef] [PubMed]

91. Chang, R.-J.; Tan, H.; Wang, X.; Porter, B.; Chen, T.; Sheng, Y.; Zhou, Y.; Huang, H.; Bhaskaran, H.; Warner, J.H. High-Performance All 2D-Layered Tin Disulfide: Graphene Photodetecting Transistors with Thickness-Controlled Interface Dynamics. *ACS Appl. Mater. Interfaces* **2018**, *10*, 13002–13010. [CrossRef] [PubMed]

92. Cong, C.; Shang, J.; Wu, X.; Cao, B.; Peimyoo, N.; Qiu, C.; Sun, L.; Yu, T. Synthesis and Optical Properties of Large-Area Single-Crystalline 2D Semiconductor WS$_2$ Monolayer from Chemical Vapor Deposition. *Adv. Opt. Mater.* **2014**, *2*, 131–136. [CrossRef]

93. Ye, G.; Gong, Y.; Lei, S.; He, Y.; Li, B.; Zhang, X.; Jin, Z.; Dong, L.; Lou, J.; Vajtai, R.; et al. Synthesis of large-scale atomic-layer SnS$_2$ through chemical vapor deposition. *Nano Res.* **2017**, *10*, 2386–2394. [CrossRef]

94. Dai, C.; Li, B.; Li, J.; Zhao, B.; Wu, R.; Ma, H.; Duan, X. Controllable synthesis of NiS and NiS$_2$ nanoplates by chemical vapor deposition. *Nano Res.* **2020**, *13*, 2506–2511. [CrossRef]

95. Ardahe, M.; Hantehzadeh, M.R.; Ghoranneviss, M. Effect of Growth Temperature on Physical Properties of MoS$_2$ Thin Films Synthesized by CVD. *J. Electron. Mater.* **2019**, *49*, 1002–1008. [CrossRef]

96. Samad, L.; Cabán-Acevedo, M.; Shearer, M.; Park, K.; Hamers, R.; Jin, S. Direct Chemical Vapor Deposition Synthesis of Phase-Pure Iron Pyrite (FeS$_2$) Thin Films. *Chem. Mater.* **2015**, *27*, 3108–3114. [CrossRef]

97. Backes, C.; Szydłowska, B.M.; Harvey, A.; Yuan, S.; Vega-Mayoral, V.; Davies, B.R.; Zhao, P.-L.; Hanlon, D.; Santos, E.J.G.; Katsnelson, M.I.; et al. Production of Highly Monolayer Enriched Dispersions of Liquid-Exfoliated Nanosheets by Liquid Cascade Centrifugation. *ACS Nano* **2016**, *10*, 1589–1601. [CrossRef]

98. Mihai, C.; Sava, F.; Galca, A.C.; Velea, A. Low power non-volatile memory switching in monolayer-rich 2D WS$_2$ and MoS$_2$ devices. *AIP Adv.* **2020**, *10*, 025102. [CrossRef]

99. Chen, T.-Y.; Chang, Y.-H.; Hsu, C.-L.; Wei, K.-H.; Chiang, C.-Y.; Li, L.-J. Comparative study on MoS$_2$ and WS$_2$ for electrocatalytic water splitting. *Int. J. Hydrogen Energy* **2013**, *38*, 12302–12309. [CrossRef]

100. Ma, L.; Chen, W.-X.; Xu, Z.-D.; Xia, J.-B.; Li, X. Carbon nanotubes coated with tubular MoS$_2$ layers prepared by hydrothermal reaction. *Nanotechnology* **2006**, *17*, 571–574. [CrossRef]

101. Li, Q.; Zhang, N.; Yang, Y.; Wang, G.; Ng, D.H.L. High Efficiency Photocatalysis for Pollutant Degradation with MoS$_2$/C$_3$N$_4$ Heterostructures. *Langmuir* **2014**, *30*, 8965–8972. [CrossRef] [PubMed]

102. Lukowski, M.A.; Daniel, A.S.; Meng, F.; Forticaux, A.; Li, L.; Jin, S. Enhanced Hydrogen Evolution Catalysis from Chemically Exfoliated Metallic MoS$_2$ Nanosheets. *J. Am. Chem. Soc.* **2013**, *135*, 10274–10277. [CrossRef]

103. Peng, Y.; Meng, Z.; Zhong, C.; Lu, J.; Yu, W.; Jia, Y.; Qian, Y. Hydrothermal synthesis and characterization of single-molecular-layer MoS$_2$ and MoSe$_2$. *Chem. Lett.* **2001**, *30*, 772–773. [CrossRef]

104. Afanasiev, P.; Xia, G.-F.; Berhault, G.; Jouguet, B.; Lacroix, M. Surfactant-Assisted Synthesis of Highly Dispersed Molybdenum Sulfide. *Chem. Mater.* **1999**, *11*, 3216–3219. [CrossRef]

105. Shanmugaratnam, S.; Velauthapillai, D.; Ravirajan, P.; Christy, A.A.; Shivatharsiny, Y. CoS$_2$/TiO$_2$ Nanocomposites for Hydrogen Production under UV Irradiation. *Materials* **2019**, *12*, 3882. [CrossRef] [PubMed]

106. Shanmugaratnam, S.; Selvaratnam, B.; Baride, A.; Koodali, R.; Ravirajan, P.; Velauthapillai, D.; Shivatharsiny, Y. SnS$_2$/TiO$_2$ Nanocomposites for Hydrogen Production and Photodegradation under Extended Solar Irradiation. *Catalysts* **2021**, *11*, 589. [CrossRef]

107. Cao, J.; Zhou, J.; Zhang, Y.; Wang, Y.; Liu, X. Dominating Role of Aligned MoS$_2$/Ni$_3$S$_2$ Nanoarrays Supported on Three-Dimensional Ni Foam with Hydrophilic Interface for Highly Enhanced Hydrogen Evolution Reaction. *ACS Appl. Mater. Interfaces* **2018**, *10*, 1752–1760. [CrossRef]

108. Gao, B.; Du, X.; Ma, Y.; Li, Y.; Li, Y.; Ding, S.; Song, Z.; Xiao, C. 3D flower-like defected MoS$_2$ magnetron-sputtered on candle soot for enhanced hydrogen evolution reaction. *Appl. Catal. Environ.* **2020**, *263*, 117750. [CrossRef]

109. Nadeem Riaz, K.; Yousaf, N.; Bilal Tahir, M.; Israr, Z.; Iqbal, T. Facile hydrothermal synthesis of 3D flower-like La-MoS$_2$ nanostructure for photocatalytic hydrogen energy production. *Int. J. Energy Res.* **2019**, *43*, 491–499. [CrossRef]

110. Radisavljevic, B.; Radenovic, A.; Brivio, J.; Giacometti, V.; Kis, A. Single-layer MoS$_2$ transistors. *Nat. Nanotechnol.* **2011**, *6*, 147–150. [CrossRef]

111. Gaur, R.; Jeevanandam, P. Synthesis of SnS$_2$ Nanoparticles and Their Application as Photocatalysts for the Reduction of Cr(VI). *J. Nanosci. Nanotechnol.* **2018**, *18*, 165–177. [CrossRef]

112. Zhu, L.; Susac, D.; Teo, M.; Wong, K.; Wong, P.; Parsons, R.; Bizzotto, D.; Mitchell, K.; Campbell, S. Investigation of CoS2-based thin films as model catalysts for the oxygen reduction reaction. *J. Catal.* **2008**, *258*, 235–242. [CrossRef]

113. Wang, J.; Yin, Y. Fermentative hydrogen production using pretreated microalgal biomass as feedstock. *Microb. Cell Factories* **2018**, *17*, 1–16. [CrossRef]

114. Kye, J.; Shin, M.; Lim, B.; Jang, J.-W.; Oh, I.; Hwang, S. Platinum Monolayer Electrocatalyst on Gold Nanostructures on Silicon for Photoelectrochemical Hydrogen Evolution. *ACS Nano* **2013**, *7*, 6017–6023. [CrossRef]

115. Mckone, J.R.; Pieterick, A.P.; Gray, H.B.; Lewis, N.S. Supporting Information: Hydrogen Evolution from Pt /Ru-Coated p-Type WSe$_2$ Photocathodes. *J. Am. Chem. Soc.* **2013**, *135*, 223–231. [CrossRef] [PubMed]

116. Wiensch, J.D.; John, J.; Velazquez, J.M.; Torelli, D.A.; Pieterick, A.P.; McDowell, M.T.; Sun, K.; Zhao, X.; Brunschwig, B.S.; Lewis, N.S. Comparative Study in Acidic and Alkaline Media of the Effects of pH and Crystallinity on the Hydrogen-Evolution Reaction on MoS$_2$ and MoSe$_2$. *ACS Energy Lett.* **2017**, *2*, 2234–2238. [CrossRef]

117. Sun, B.; Wang, H.; Wu, J.; Geng, Y.; Xu, J.; Wang, Y.; Li, Y.; Lin, H.; Wang, L. Designed synthesis of unique ZnS@CdS@Cd$_{0.5}$Zn$_{0.5}$S-MoS$_2$ hollow nanospheres for efficient visible-light-driven H$_2$ evolution. *CrystEngComm* **2020**, *22*, 2743–2755. [CrossRef]

118. Komba, N.; Zhang, G.; Pu, Z.; Wu, M.; Rosei, F.; Sun, S. MoS$_2$-supported on free-standing TiO$_2$-nanotubes for efficient hydrogen evolution reaction. *Int. J. Hydrogen Energy* **2020**, *45*, 4468–4480. [CrossRef]

119. Zhao, X.; Ma, X.; Sun, J.; Li, D.; Yang, X. Enhanced Catalytic Activities of Surfactant-Assisted Exfoliated WS$_2$ Nanodots for Hydrogen Evolution. *ACS Nano* **2016**, *10*, 2159–2166. [CrossRef] [PubMed]

120. Mao, Q.; Chen, J.; Chen, H.; Chen, Z.; Chen, J.; Li, Y. Few-layered 1T-MoS$_2$-modified ZnCoS solid-solution hollow dodecahedra for enhanced photocatalytic hydrogen evolution. *J. Mater. Chem. A* **2019**, *7*, 8472–8484. [CrossRef]

121. Oertel, M.; Schmitz, J.; Weirich, W.; Jendryssek-Neumann, D.; Schulten, R. Vapour-liquid Equilibrium Data Collec-tion' dechema Frankfurt. *Izv. Vyss. Uchebn. Zaved. Khim. Tekhnol.* **1987**, *27*, 686–691.

122. Kumar, S.S.; Himabindu, V. Hydrogen production by PEM water electrolysis—A review. *Mater. Sci. Energy Technol.* **2019**, *2*, 442–454. [CrossRef]

123. Dehghanimadvar, M.; Shirmohammadi, R.; Sadeghzadeh, M.; Aslani, A.; Ghasempour, R. Hydrogen production technologies: Attractiveness and future perspective. *Int. J. Energy Res.* **2020**, *44*, 8233–8254. [CrossRef]

124. FreedomCAR and Fuel Partnership Hydrogen Offers Sustainable Solutions to Our Nation's Energy and Climate Challenges. Table of Contents Sustainability Urban Air Quality. 2009. Available online: https://www1.eere.energy.gov/hydrogenandfuelcells/pdfs/h2_tech_roadmap.pdf (accessed on 11 October 2021).

125. Luo, X.; Wu, T.; Shi, K.; Song, M.; Rao, Y. Biomass Gasification: An Overview of Technological Barriers and Socio-Environmental Impact. *Gasif. Low-Grade Feedstock* **2018**, 3–18. [CrossRef]

126. Ding, Q.; Song, B.; Xu, P.; Jin, S. Efficient Electrocatalytic and Photoelectrochemical Hydrogen Generation Using MoS$_2$ and Related Compounds. *Chem* **2016**, *1*, 699–726. [CrossRef]

127. Chu, D.; Zhang, C.; Yang, P.; Du, Y.; Lu, C. WS$_2$ as an Effective Noble-Metal Free Cocatalyst Modified TiSi$_2$ for Enhanced Photocatalytic Hydrogen Evolution under Visible Light Irradiation. *Catalysts* **2016**, *6*, 136. [CrossRef]

128. Zhang, J.; Hu, W.; Cao, S.; Piao, L. Recent progress for hydrogen production by photocatalytic natural or simulated seawater splitting. *Nano Res.* **2020**, *13*, 2313–2322. [CrossRef]

129. Liu, J.; Yu, G.; Zhang, R.; Huang, X.; Chen, W. Theoretical predication of the high hydrogen evolution catalytic activity for the cubic and tetragonal SnP systems. *Phys. Chem. Chem. Phys.* **2019**, *21*, 5521–5530. [CrossRef] [PubMed]

130. Som, N.N.; Jha, P.K. Hydrogen evolution reaction of metal di-chalcogenides: ZrS$_2$, ZrSe$_2$ and Janus ZrSSe. *Int. J. Hydrogen Energy* **2020**, *45*, 23920–23927. [CrossRef]

131. Wang, B.; Wang, X.; Yuan, H.; Zhou, T.; Chang, J.; Chen, H. Direct Z-scheme photocatalytic overall water splitting on two dimensional MoSe$_2$/SnS$_2$ heterojunction. *Int. J. Hydrogen Energy* **2020**, *45*, 2785–2793. [CrossRef]

132. Park, H.; Akande, A.; Sanvito, S.; El-Mellouhi, F. The rise of Nb-, Ta-, and Bi-based oxides/chalcogenides for photocatalytic applications. *Int. J. Hydrogen Energy* **2021**, 1–13. [CrossRef]

133. Ran, N.; Qiu, W.; Song, E.; Wang, Y.; Zhao, X.; Liu, Z.; Liu, J. Bond Electronegativity as Hydrogen Evolution Reaction Catalyst Descriptor for Transition Metal (TM = Mo, W) Dichalcogenides. *Chem. Mater.* **2020**, *32*, 1224–1234. [CrossRef]

134. Faraji, M.; Yousefi, M.; Yousefzadeh, S.; Zirak, M.; Naseri, N.; Jeon, T.H.; Choi, W.; Moshfegh, A.Z. Two-dimensional materials in semiconductor photoelectrocatalytic systems for water splitting. *Energy Environ. Sci.* **2019**, *12*, 59–95. [CrossRef]

135. Huang, D.; Wen, M.; Zhou, C.; Li, Z.; Cheng, M.; Chen, S.; Xue, W.; Lei, L.; Yang, Y.; Xiong, W.; et al. Zn$_x$Cd$_{1-x}$S based materials for photocatalytic hydrogen evolution, pollutants degradation and carbon dioxide reduction. *Appl. Catal. Environ.* **2020**, *267*, 118651. [CrossRef]

136. Kudo, A.; Kato, H.; Tsuji, I. Strategies for the Development of Visible-light-driven Photocatalysts for Water Splitting. *Chem. Lett.* **2004**, *33*, 1534–1539. [CrossRef]

137. Li, K.; Li, Y.; Wang, Y.; Ge, J.; Liu, C.; Xing, W. Enhanced electrocatalytic performance for the hydrogen evolution reaction through surface enrichment of platinum nanoclusters alloying with ruthenium in situ embedded in carbon. *Energy Environ. Sci.* **2018**, *11*, 1232–1239. [CrossRef]
138. Ahn, S.; Yang, J.; Lim, H.; Shin, H.S. Selective synthesis of pure cobalt disulfide on reduced graphene oxide sheets and its high electrocatalytic activity for hydrogen evolution reaction. *Nano Converg.* **2016**, *3*, 1–7. [CrossRef] [PubMed]
139. Gao, C.; Hua, H.; Du, M.; Liu, J.; Wu, X.; Pu, Y.; Li, X. 1T/2H MoS_2 nanoflowers decorated amorphous Mo-CoS_x skeleton: A ZIF-based composite electrocatalyst for the hydrogen evolution reaction. *Appl. Surf. Sci.* **2020**, *515*, 145842. [CrossRef]
140. Bhat, K.S.; Nagaraja, H. Performance evaluation of molybdenum dichalcogenide (MoX2; X= S, Se, Te) nanostructures for hydrogen evolution reaction. *Int. J. Hydrogen Energy* **2019**, *44*, 17878–17886. [CrossRef]
141. Li, H.; Yang, C.; Wang, X.; Zhang, J.; Xi, J.; Du, G.; Ji, Z. Mixed 3D/2D dimensional TiO_2 nanoflowers/$MoSe_2$ nanosheets for enhanced photoelectrochemical hydrogen generation. *J. Am. Ceram. Soc.* **2020**, *103*, 1187–1196. [CrossRef]
142. Sharma, M.D.; Mahala, C.; Basu, M. 2D Thin Sheet Heterostructures of MoS_2 on $MoSe_2$ as Efficient Electrocatalyst for Hydrogen Evolution Reaction in Wide pH Range. *Inorg. Chem.* **2020**, *59*, 4377–4388. [CrossRef]
143. Xia, Y.; Wu, W.; Wang, H.; Rao, S.; Zhang, F.; Zou, G. Amorphous RuS_2 electrocatalyst with optimized active sites for hydrogen evolution. *Nanotechnology* **2020**, *31*, 145401. [CrossRef] [PubMed]
144. Zhang, D.; Mou, H.; Chen, L.; Wang, D.; Song, C. Design and in-situ synthesis of unique catalyst via embedding graphene oxide shell membrane in NiS_2 for efficient hydrogen evolution. *Appl. Surf. Sci.* **2020**, *510*, 145483. [CrossRef]
145. Manjunathaae, C.; Patil, R.S.; Sudeep, M.; Srinivasa, N.; Kumar, R.C.; Aan, M.S.; Ashoka, S. Rational design and synthesis of hetero-nanostructured electrospun PU@PANI@FeS_2: A surface tailored hybrid catalyst for H_2 production via electrochemical splitting of water. *Surf. Interfaces* **2020**, *18*, 100445. [CrossRef]
146. Zeng, X.; Jiao, Q.; Li, N.; Wang, J. Facile synthesis of CuxS coated electrodes for the efficient hydrogen evolution reaction. *Appl. Surf. Sci.* **2020**, *513*, 145785. [CrossRef]
147. Li, Z.; Liu, P.; Yang, G. Efficient All-2D Amorphous Cobalt Sulfide Nanosheets/Multilayered Molybdenum Disulfide Hybrid Heterojunction Catalyst for Electrochemical Hydrogen Evolution. *Glob. Chall.* **2020**, *4*, 1900066. [CrossRef] [PubMed]
148. Zhu, X.; Dai, J.; Li, L.; Zhao, D.; Wu, Z.; Tang, Z.; Ma, L.-J.; Chen, S. Hierarchical carbon microflowers supported defect-rich Co3S4 nanoparticles: An efficient electrocatalyst for water splitting. *Carbon* **2020**, *160*, 133–144. [CrossRef]
149. Aslan, E.; Sarilmaz, A.; Yanalak, G.; Chang, C.S.; Cinar, I.; Ozel, F.; Patir, I.H. Facile preparation of amorphous NiWSex and CoWSex nanoparticles for the electrocatalytic hydrogen evolution reaction in alkaline condition. *J. Electroanal. Chem.* **2019**, *856*, 113674. [CrossRef]
150. Li, G.; Chen, Z.; Li, Y.; Zhang, D.; Yang, W.; Liu, Y.; Cao, L. Engineering Substrate Interaction to Improve Hydrogen Evolution Catalysis of Monolayer MoS_2 Films beyond Pt. *ACS Nano* **2020**, *14*, 1707–1714. [CrossRef] [PubMed]
151. Nguyen, V.-T.; Le, P.A.; Hsu, Y.-C.; Wei, K.-H. Plasma-Induced Exfoliation Provides Onion-Like Graphene-Surrounded MoS_2 Nanosheets for a Highly Efficient Hydrogen Evolution Reaction. *ACS Appl. Mater. Interfaces* **2020**, *12*, 11533–11542. [CrossRef] [PubMed]
152. Shi, Q.; Zhou, Y.; Sun, W.; Wang, H.; Li, S.; Zhang, X.; Wan, J. Hydrogen Evolution and Wastewater Treatment of Hydrangeal-like Catalyst Decroatedby the NiS Nanosheet and PdNanoparticle. *ChemistrySelect* **2020**, *5*, 1041–1046. [CrossRef]
153. Zhao, A.; Zhang, L.; Xu, G.; Zhang, X.; Zhang, S.; Xiao, Y. Hollow $Zn_xCo_{1-x}Se_2$ microcubes derived from Metal–Organic framework as efficient bifunctional electrocatalysts for hydrogen evolution and oxygen evolution reactions. *Int. J. Hydrogen Energy* **2020**, *45*, 2607–2616. [CrossRef]
154. Zhou, Y.; Zhang, J.; Ren, H.; Pan, Y.; Yan, Y.; Sun, F.; Wang, X.; Wang, S.; Zhang, J. Mo doping induced metallic CoSe for enhanced electrocatalytic hydrogen evolution. *Appl. Catal. B Environ.* **2020**, *268*, 118467. [CrossRef]
155. Liang, Y.; Yang, Y.; Xu, K.; Yu, T.; Yao, S.; Peng, Q.; Yuan, C. Crystal plane dependent electrocatalytic performance of NiS_2 nanocrystals for hydrogen evolution reaction. *J. Catal.* **2020**, *381*, 63–69. [CrossRef]
156. Friedman, F.; Hastie, T.; John, T.; Weatherwax, R.L.; Epstein, D.; Wasserman, L.; Abu-El-Haija, S.; Do, C.B.; Batzoglou, S.; Resknik, C.; et al. Solution-processed GaSe nanoflake-based films for photoelectrochemical water splitting and photoelectrochemical-type. *J. Chem. Inf. Model.* **2013**, *67*, 1689–1699. [CrossRef]
157. Ma, F.; Liang, Y.; Zhou, P.; Tong, F.; Wang, Z.; Wang, P.; Liu, Y.; Dai, Y.; Zheng, Z.; Huang, B. One-step synthesis of Co-doped 1T-MoS_2 nanosheets with efficient and stable HER activity in alkaline solutions. *Mater. Chem. Phys.* **2020**, *244*, 122642. [CrossRef]
158. Song, W.; Wang, K.; Jin, G.; Wang, Z.; Li, C.; Yang, X.; Chen, C. Two-Step Hydrothermal Synthesis of CoSe/MoSe 2 as Hydrogen Evolution Electrocatalysts in Acid and Alkaline Electrolytes. *ChemElectroChem* **2019**, *6*, 4842–4847. [CrossRef]
159. Yang, J.-X.; Yu, W.-B.; Li, C.-F.; Dong, W.-D.; Jiang, L.-Q.; Zhou, N.; Zhuang, Z.-P.; Liu, J.; Hu, Z.-Y.; Zhao, H.; et al. PtO nanodots promoting Ti3C2 MXene in-situ converted Ti3C2/TiO_2 composites for photocatalytic hydrogen production. *Chem. Eng. J.* **2021**, *420*, 129695. [CrossRef]
160. Guayaquil-Sosa, J.; Rosales, B.S.; Valadés-Pelayo, P.; De Lasa, H. Photocatalytic hydrogen production using mesoporous TiO_2 doped with Pt. *Appl. Catal. Environ.* **2017**, *211*, 337–348. [CrossRef]
161. Zhao, H.; Li, C.-F.; Hu, Z.-Y.; Liu, J.; Li, Y.; Hu, J.; Van Tendeloo, G.; Chen, L.-H.; Su, B.-L. Size effect of bifunctional gold in hierarchical titanium oxide-gold-cadmium sulfide with slow photon effect for unprecedented visible-light hydrogen production. *J. Colloid Interface Sci.* **2021**, *604*, 131–140. [CrossRef] [PubMed]

162. Yerga, R.M.N.; Alvarez-Galvan, M.C.; Del Valle, F.; De La Mano, J.A.V.; Fierro, J.L.G. Water Splitting on Semiconductor Catalysts under Visible-Light Irradiation. *ChemSusChem* **2009**, *2*, 471–485. [CrossRef] [PubMed]

163. Wang, Q.; Huang, J.; Sun, H.; Zhang, K.-Q.; Lai, Y. Uniform carbon dots@TiO$_2$ nanotube arrays with full spectrum wavelength light activation for efficient dye degradation and overall water splitting. *Nanoscale* **2017**, *9*, 16046–16058. [CrossRef]

164. Onsuratoom, S.; Chavadej, S.; Sreethawong, T. Hydrogen production from water splitting under UV light irradiation over Ag-loaded mesoporous-assembled TiO$_2$–ZrO$_2$ mixed oxide nanocrystal photocatalysts. *Int. J. Hydrogen Energy* **2011**, *36*, 5246–5261. [CrossRef]

165. Chen, J.; Wu, X.-J.; Yin, L.; Li, B.; Hong, X.; Fan, Z.; Chen, B.; Xue, C.; Zhang, H. One-pot Synthesis of CdS Nanocrystals Hybridized with Single-Layer Transition-Metal Dichalcogenide Nanosheets for Efficient Photocatalytic Hydrogen Evolution. *Angew. Chem. Int. Ed.* **2015**, *54*, 1210–1214. [CrossRef]

166. Zong, X.; Han, J.; Ma, G.; Yan, H.; Wu, G.; Li, C. Photocatalytic H$_2$ Evolution on CdS Loaded with WS$_2$ as Cocatalyst under Visible Light Irradiation. *J. Phys. Chem. C* **2011**, *115*, 12202–12208. [CrossRef]

167. Ran, J.; Zhang, J.; Yu, J.; Jaroniec, M.; Qiao, S.Z. Earth-abundant cocatalysts for semiconductor-based photocatalytic water splitting. *Chem. Soc. Rev.* **2014**, *43*, 7787–7812. [CrossRef] [PubMed]

168. Yan, C.; Xue, X.; Zhang, W.; Li, X.; Liu, J.; Yang, S.; Hu, Y.; Chen, R.; Yan, Y.; Zhu, G.; et al. Well-designed Te/SnS$_2$/Ag artificial nanoleaves for enabling and enhancing visible-light driven overall splitting of pure water. *Nano Energy* **2017**, *39*, 539–545. [CrossRef]

169. Liu, E.; Chen, J.; Ma, Y.; Feng, J.; Jia, J.; Fan, J.; Hu, X. Fabrication of 2D SnS$_2$/g-C$_3$N$_4$ heterojunction with enhanced H$_2$ evolution during photocatalytic water splitting. *J. Colloid Interface Sci.* **2018**, *524*, 313–324. [CrossRef] [PubMed]

170. Ke, X.; Dai, K.; Zhu, G.; Zhang, J.; Liang, C. In situ photochemical synthesis noble-metal-free NiS on CdS-diethylenetriamine nanosheets for boosting photocatalytic H2 production activity. *Appl. Surf. Sci.* **2019**, *481*, 669–677. [CrossRef]

171. Khan, Z.; Chetia, T.R.; Vardhaman, A.K.; Barpuzary, D.; Sastri, C.V.; Qureshi, M. Visible light assisted photocatalytic hydrogen generation and organic dye degradation by CdS–metal oxide hybrids in presence of graphene oxide. *RSC Adv.* **2012**, *2*, 12122–12128. [CrossRef]

172. Chang, K.; Mei, Z.; Wang, T.; Kang, Q.; Ouyang, S.; Ye, J. MoS$_2$/Graphene Cocatalyst for Efficient Photocatalytic H2 Evolution under Visible Light Irradiation. *ACS Nano* **2014**, *8*, 7078–7087. [CrossRef]

173. Jiang, D.; Zhu, L.; Irfan, R.M.; Zhang, L.; Du, P. Integrating noble-metal-free NiS cocatalyst with a semiconductor heterojunction composite for efficient photocatalytic H 2 production in water under visible light. *Chin. J. Catal.* **2017**, *38*, 2102–2109. [CrossRef]

174. Xin, X.; Song, Y.; Guo, S.; Zhang, Y.; Wang, B.; Yu, J.; Li, X. In-situ growth of high-content 1T phase MoS$_2$ confined in the CuS nanoframe for efficient photocatalytic hydrogen evolution. *Appl. Catal. Environ.* **2020**, *269*, 118773. [CrossRef]

175. Nagappagari, L.R.; Samanta, S.; Sharma, N.; Battula, V.R.; Kailasam, K. Synergistic effect of a noble metal free Ni(OH)$_2$ co-catalyst and a ternary ZnIn2S4/g-C3N4 heterojunction for enhanced visible light photocatalytic hydrogen evolution. *Sustain. Energy Fuels* **2020**, *4*, 750–759. [CrossRef]

176. Guo, X.; Guo, P.; Wang, C.; Chen, Y.; Guo, L. Few-layer WSe$_2$ nanosheets as an efficient cocatalyst for improved photocatalytic hydrogen evolution over Zn$_{0.1}$Cd$_{0.9}$S nanorods. *Chem. Eng. J.* **2020**, *383*, 123183. [CrossRef]

177. Li, Y.; Zhang, D.; Xi, X.; Shen, Y.; Chang, S.; Zhu, J.; Chen, Y.; Jiang, L.; Zhang, J. Noble metal-free bimetallic NiCo decorated Zn$_{0.5}$Cd$_{0.5}$S solid solution for enhanced photocatalytic H2 evolution under visible light. *Int. J. Hydrogen Energy* **2020**, *45*, 8300–8309. [CrossRef]

178. Jia, J.; Bai, X.; Zhang, Q.; Hu, X.; Liu, E.; Fan, J. Porous honeycomb-like NiSe2/red phosphorus heteroarchitectures for photocatalytic hydrogen production. *Nanoscale* **2020**, *12*, 5636–5651. [CrossRef] [PubMed]

179. Zhu, Y.; Chen, J.; Shao, L.; Xia, X.; Liu, Y.; Wang, L. Oriented facet heterojunctions on CdS nanowires with high photoactivity and photostability for water splitting. *Appl. Catal. B Environ.* **2020**, *268*, 118744. [CrossRef]

180. Han, J.; Liu, Y.; Wang, Y.; Zhao, R.; Wang, L. Construction of ternary CdxMo1−xSe quantum dots for enhanced photocatalytic hydrogen production. *J. Mater. Sci.* **2019**, *55*, 1117–1125. [CrossRef]

181. Beall, C.; Piipari, K.; Al-qassab, H.; Smith, M.A. MoS$_2$/CdIn$_2$S$_4$ flower-like heterojunctions with enhanced photocatalytic degradation and H$_2$ evolution activity. *Biochem. J.* **2010**, *53*, 1–14. [CrossRef]

182. Mangiri, R.; Reddy, D.A.; Subramanyam, K.; Kumar, K.S.; Sudharani, A.; Poornaprakash, B.; Vijayalakshmi, R. Decorating MoS$_2$ and CoSe$_2$ nanostructures on 1D-CdS nanorods for boosting photocatalytic hydrogen evolution rate. *J. Mol. Liq.* **2019**, *289*, 2–11. [CrossRef]

183. Wang, B.; Ding, Y.; Deng, Z.; Li, Z. Rational design of ternary NiS/CQDs/ZnIn$_2$S$_4$ nanocomposites as efficient noble-metal-free photocatalyst for hydrogen evolution under visible light. *Chin. J. Catal.* **2019**, *40*, 335–342. [CrossRef]

184. Chen, Z.; Gong, H.; Liu, Q.; Song, M.; Huang, C. NiSe2 Nanoparticles Grown in Situ on CdS Nanorods for Enhanced Photocatalytic Hydrogen Evolution. *ACS Sustain. Chem. Eng.* **2019**, *7*, 16720–16728. [CrossRef]

185. Yan, A.; Shi, X.; Huang, F.; Fujitsuka, M.; Majima, T. Efficient photocatalytic H$_2$ evolution using NiS/ZnIn$_2$S$_4$ heterostructures with enhanced charge separation and interfacial charge transfer. *Appl. Catal. Environ.* **2019**, *250*, 163–170. [CrossRef]

186. Rangappa, A.P.; Kumar, D.P.; Gopannagari, M.; Reddy, D.A.; Hong, Y.; Kim, Y.; Kim, T.K. Highly efficient hydrogen generation in water using 1D CdS nanorods integrated with 2D SnS$_2$ nanosheets under solar light irradiation. *Appl. Surf. Sci.* **2020**, *508*, 144803. [CrossRef]

187. Ranjith, K.S.; Kumar, D.R.; Huh, Y.S.; Shanmugam, R.K.; Uyar, T.; Kumar, R.T.R. Promotional Effect of Cu_2S–ZnS Nanograins as a Shell Layer on ZnO Nanorod Arrays for Boosting Visible Light Photocatalytic H_2 Evolution. *J. Phys. Chem. C* **2020**, *124*, 3610–3620. [CrossRef]

188. Puentes-Prado, E.; Garcia, C.; Oliva, J.; Galindo, R.; Bernal-Alvarado, J.; Torres, L.D.; Gomez-Solis, C. Enhancing the solar photocatalytic hydrogen generation of ZnS films by UV radiation treatment. *Int. J. Hydrogen Energy* **2020**, *45*, 12308–12317. [CrossRef]

189. Li, X.; Song, S.; Gao, Y.; Ge, L.; Song, W.; Ma, T.; Liu, J. Identification of the Charge Transfer Channel in Cobalt Encapsulated Hollow Nitrogen-Doped Carbon Matrix@CdS Heterostructure for Photocatalytic Hydrogen Evolution. *Small* **2021**, *17*, 2101315. [CrossRef]

190. Zhang, Z.; Kang, Y.; Yin, L.-C.; Niu, P.; Zhen, C.; Chen, R.; Kang, X.; Wu, F.; Liu, G. Constructing CdSe QDs modified porous g-C_3N_4 heterostructures for visible light photocatalytic hydrogen production. *J. Mater. Sci. Technol.* **2021**, *95*, 167–171. [CrossRef]

191. Wong, K.-L.; Bünzli, J.-C.G.; Tanner, P.A. Quantum yield and brightness. *J. Lumin.* **2020**, *224*, 117256. [CrossRef]

192. Bouas-Laurent, H.; Dürr, H. Organic photochromism (IUPAC Technical Report) Republication or reproduction of this report or its storage and/or dissemination by electronic means is permitted without the need for formal IUPAC permission on condition that an acknowledgment, with full re. *Photochromism* **2003**, *73*, 639–665. [CrossRef]

193. Meng, X.; Zhang, C.; Dong, C.; Sun, W.; Ji, D.; Ding, Y. Carbon quantum dots assisted strategy to synthesize Co@NC for boosting photocatalytic hydrogen evolution performance of CdS. *Chem. Eng. J.* **2020**, *389*, 124432. [CrossRef]

194. Yuan, Y.; Lu, H.; Ji, Z.; Zhong, J.; Ding, M.; Chen, D.; Li, Y.; Tu, W.; Cao, D.; Yu, Z.; et al. Enhanced visible-light-induced hydrogen evolution from water in a noble-metal-free system catalyzed by ZnTCPP-MoS_2/TiO_2 assembly. *Chem. Eng. J.* **2015**, *275*, 8–16. [CrossRef]